

## ABSTRACT

SUTTON, MARGARET TURNER. ENSO-Driven Impacts on Wintertime Climate Anomalies Over North America. (Under the direction of Dr. Sarah Larson).

Enhanced sea surface temperature variability in the equatorial eastern Pacific due to the El Niño-Southern Oscillation (ENSO) forces an extratropical large-scale atmospheric response. The atmospheric response drives immense climate impacts across the globe. The degree to which the atmospheric circulation is altered due to ENSO is the subject of this study. Two multi-century, CESM1-CAM4 simulations are compared: a fully coupled experiment (CTRL), and a partially decoupled experiment (NoENSO). In the NoENSO experiment, the anomalous wind stress coupling in the equatorial Pacific is disengaged, deactivating the Bjerknes Feedback, thus dampening ENSO variability. The percent difference equation is used to quantitatively compare the experiments and assess the impact of ENSO on upper-level and surface features, specifically in 500hPa geopotential height, upper-level winds, and precipitation. Results suggest that ENSO preferentially drives interannual variance to the northern and southern regions of North America causing a significant displacement of interannual variance to occur over central North America in 500hPa geopotential heights and 200hPa zonal wind variability. At the surface, ENSO enhances interannual precipitation variance in the southeastern region of the United States and reduces interannual variance in an adjacent region south of the Great Lakes, thus displacing variability from the southeast towards the northwest. However, due to large internal variability, sampling variability plays a critical role in understanding and resolving the atmospheric forced response to ENSO. A limited observational record and short simulation lengths can lead to a less comprehensive understanding of ENSO impacts due to the undersampling of ENSO neutral events. A Monte Carlo random sampling method is used to determine the minimum number of

ENSO neutral years needed to estimate the impact of ENSO variability on 500hPa geopotential height and precipitation variance within 10% uncertainty. Then, an extrapolation method is used to determine the total simulation length needed to resolve ENSO teleconnections in the CTRL experiment. The results imply that a substantially longer record is needed to accurately depict ENSO's teleconnections than suggested in previous studies.

© Copyright 2021 by Margaret Sutton

All Rights Reserved

ENSO-Driven Impacts on Wintertime Climate Anomalies Over North America

by  
Margaret Sutton

A thesis submitted to the Graduate Faculty of  
North Carolina State University  
in partial fulfillment of the  
requirements for the degree of  
Master of Science

Marine, Earth & Atmospheric Sciences

Raleigh, North Carolina

2021

APPROVED BY:

---

Dr. Sarah Larson  
Committee Chair

---

Dr. Walter Robinson

---

Dr. Anantha Aiyyer

## **DEDICATION**

This thesis is dedicated to, Cynthia Pierce, my Calculus instructor, who encouraged and inspired me to pursue an interest in Mathematics.

## **BIOGRAPHY**

Margaret Sutton was born and spent the formative years of her life in Raleigh, NC. During her junior year of high school, she moved to her ancestral home in Windsor, NC, located in the Innerbanks of NC. She earned a Bachelor of Science in Mathematics at Greensboro College with a minor in Spanish. During her time at Greensboro College, she was the Captain of the Greensboro College Swim Team, Vice President of the Iota Iota Chapter of Alpha Xi Delta Sorority, a Resident Advisor, Public Relations Chair in the Student Government Association, and served on the Dean's Advisory Council. During Fall 2016, her senior year of college, Hurricane Matthew hit the coast of North Carolina. The damage associated with Hurricane Matthew was great and left much of the small town of Windsor under water. Businesses were forced to close indefinitely, and many Windsor residents lost their homes. Over the past decades, Windsor has experience four major floods, reaching 100-year and 500-year flood levels. The increase in detrimental flooding in Windsor and the connection with hurricane activity is what influenced the shift in her career path to apply her mathematical background to investigate the impact of the main source of climate variability over North America.

## **ACKNOWLEDGMENTS**

I would like to acknowledge my advisor, Dr. Sarah Larson, for the guidance and advice throughout pursuing my master's degree. My committee members, Drs. Anantha Aiyyer and Walter Robinson, for the time they have taken to support this work and their guidance in the direction of this project. I would like to thank my fellow Climate Modeling and Predictability Research Group members, Mahdi Hasan, Kay McMonigal, and Sam Michlowitz, for their invaluable support and guidance. On top of pursuing their own degrees, they took ample time out of their schedule to ensure my success, specifically during the last few months leading up to my master's research defense. Lastly, I would like to thank my family, friends, and partner for their encouragement and understanding during this process.

# TABLE OF CONTENTS

LIST OF FIGURES .....	vi
<b>Chapter 1: Introduction</b> .....	<b>1</b>
1.1. What is ENSO? .....	1
1.2. ENSO Impacts on the Overlying Atmosphere .....	3
1.3. ENSO Impacts on the Extra-tropics .....	5
1.4. Quantifying ENSO’s Impacts on Climate Variability .....	6
<b>Chapter 2: Data and Analysis Methods</b> .....	<b>9</b>
2.1. Observational Datasets .....	9
2.2. Model Description and Validation .....	10
2.2.1. Community Earth System Model Version 1 – Community Atmospheric Model Version 4 .....	11
2.2.2. Community Earth System Model Version 2 .....	13
2.3. Analysis Methods .....	14
<b>Chapter 3: Model Experiments and Validation</b> .....	<b>16</b>
3.1. CTRL Experiment .....	16
3.1.1. CTRL Mean State Comparison to Observations .....	16
3.1.2. ENSO Variability Comparison to Observations .....	18
3.2. NoENSO Experiment .....	22
3.2.1. Experimental Design .....	22
3.2.2. NoENSO Mean State Comparison to CTRL .....	24
3.2.3. ENSO Variability Comparison to CTRL .....	26
<b>Chapter 4: Result: ENSO Impacts</b> .....	<b>45</b>
4.1. Interannual SST Variability .....	45
4.2. Interannual Atmospheric Circulation Variability .....	46
4.2.1. Interannual 500 hPa Geopotential Height Variability .....	46
4.2.2. Interannual 200 hPa Zonal Wind Variability .....	48
4.3. Interannual Surface Variability .....	49
4.3.1. Interannual Precipitation Variability .....	49
<b>Chapter 5: Result: Sensitivity to Sample Size</b> .....	<b>60</b>
5.1. Can the Model-Derived Signal be Obtained from Observations? .....	60
5.2. Sensitivity to the ENSO-neutral Threshold .....	62
5.3. Sensitivity to Sampling Variability .....	64
5.4. Testing the Sample Size Hypothesis .....	67
<b>Chapter 6: Summary and Conclusions</b> .....	<b>77</b>
REFERENCES .....	83

## LIST OF FIGURES

Figure 3.1	Seasonally averaged DJF SST Climatology. Units are °C. Top: CTRL experiment with 322 simulated years. Bottom: ERSST.v5 Reanalysis Data from 1980-2020. The ERSST.v5 has been detrended for accurate comparison with CTRL experiment.....	28
Figure 3.2	Zonal Seasonal SST Climatology across the equatorial Pacific Ocean (5°N-5°S, 120°E-60°W) in °C. Solid lines: Seasonal SST from the CESM1-CAM4. Dashed lines: Seasonal SST found in the ERSST.v5.....	29
Figure 3.3	Seasonally averaged DJF Z500 Climatology. Units are in meters. Top: CESM1-CAM4 CTRL experiment with 322 simulated years. Bottom: NCEP Reanalysis Data from 1980-2020. The NCEP dataset has been detrended for accurate comparison with CTRL experiment. ....	30
Figure 3.4	Seasonally averaged DJF U200 Climatology. Units are in m/s. Red shading is indicative of westerly winds speeds and blue shading represents easterly wind speeds. Top: CESM1-CAM4 CTRL experiment with 322 simulated years. Bottom: NCEP Reanalysis Data from 1980-2020. The NCEP dataset has been detrended for accurate comparison with CTRL experiment .....	31
Figure 3.5	Area-averaged monthly SST anomalies over the Nino3.4 Region (5°N-5°S, 120°-170°W). Units are in °C. Blue line is the Nino3.4 Index calculated by the CESM1-CAM4 CTRL run. The orange line is the Nino3.4 time series from 1980-2020.....	32
Figure 3.6	Autocorrelation of the Nino3.4 time series calculated using the area-averaged monthly seasonal SST anomalies over the Nino3.4 Region (5°N-5°S, 120°-170°W). Blue line is the autocorrelation of the CESM1-CAM4 CTRL experiment, only 40 simulated years are shown in this figure. The orange line is the Nino3.4 time series from 1980-2020. ....	33
Figure 3.7	Power Spectrum with units °C <sup>2</sup> /(cycles month <sup>-1</sup> ) of the Nino3.4 SST Index calculated using the area-averaged monthly SST anomalies over the Nino3.4 Region (5°N-5°S, 120°-170°W). Blue line is the average spectra over 35-year segments from the CTRL experiment with 300 simulated years. The orange line is the detrended average spectra from 2 35-year segments from the ERSST.v5 1950-2020.....	34
Figure 3.8	DJF SST ENSO composite anomalies are categorized based on a 0.5°C threshold. Anomalies are formed by removing the monthly mean SST from the CTRL experiment for a close comparison with observations. Units are in °C. Red shading shows warmer than average surface temperatures and blue shading indicates cooler than average surface temperatures. El Niño composites are the	

top figures and La Niña composites are shown on the bottom. Left: Detrended ERSST.v5 data from 1950-2020. Right: CTRL experiment using 322 years of simulated data.....	35
Figure 3.9 DJF Z500 ENSO composite anomalies are categorized based on a 0.5°C threshold. Anomalies are formed by removing the monthly mean Z500 from the CTRL experiment to closely compare with observations. Units are in meters. El Niño composites are the top figures and La Niña composites are shown on the bottom. Red shading shows higher than average heights and blue shading indicates lower than average heights. Left: Detrended NCEP Reanalysis data from 1950-2020. Right: CTRL experiment using 322 years of simulated data.....	36
Figure 3.10 DJF U200 ENSO composite anomalies are categorized based on a 0.5°C threshold. Anomalies are formed by removing the monthly mean U200 from the CTRL experiment to closely compare with observations. Units are in m/s. El Niño composites are the top figures and La Niña composites are shown on the bottom. Red shading shows stronger than average winds speeds and blue shading indicates weaker than average wind speeds. Left: Detrended NCEP Reanalysis data from 1950-2020. Right: CTRL experiment using 322 years of simulated data.....	37
Figure 3.11 The global wind stress mask applied to the ocean component of the CESM1-CAM4. White: All the seasonally varying anomalous wind stress and the average monthly climatological wind stress can force the ocean component. Yellow: 75% of the seasonally varying anomalous wind stress and the average monthly climatological wind stress can force the ocean component. Orange: 50% of the seasonally varying anomalous wind stress and the average monthly climatological wind stress can force the ocean component. Red: 0% of the seasonally varying anomalous wind stress and the average monthly climatological wind stress can force the ocean component, only the seasonally varying climatology is felt by the ocean. ....	38
Figure 3.12 Area-averaged monthly SST anomalies over the Nino3.4 Region (5°N-5°S, 120°-170°W). Units are in °C. Blue line is the Nino3.4 Index calculated by the CTRL run. The orange line is the Nino3.4 time series from the NoENSO run. ....	39
Figure 3.13 Annual cycle of SST averaged over the Nino3.4 region (5°N-5°S, 120°-170°W). Units are °C. Solid Black line is annual cycle from the CTRL. Dashed Red line is the annual cycle from the NoENSO. ....	40
Figure 3.14 December-January-February (DJF) seasonal SST Climatology from the CESM1-CAM4. Units are °C. Top: CTRL experiment with 322 years Bottom: NoENSO experiment with 304 years. ....	41

Figure 3.15	Difference (NoENSO-CTRL) between seasonal DJF SST Climatology across the equatorial Pacific basin (30°N-30°S,120°E-60°W). Units are °C. Red: Warmer SST in the NoENSO experiment. Blue: Cooler SST in the NoENSO experiment.....	42
Figure 3.16	Zonal seasonal CTRL and NoENSO SST Climatologies across the equatorial Pacific (5°N-5°S, 120°E-60°W). Solid lines are seasonal averages from the CTRL. Dashed lines are seasonal averages from the NoENSO. Units are °C. ....	43
Figure 3.17	DJF Z500 El Niño and La Niña composite anomalies at the latitude 96°W. Units are meters. Red line is the El Niño composite anomaly. Blue line is the La Niña composite anomaly. Left: Composite anomalies calculated using the monthly mean from the CTRL. Right: Composite anomalies calculated using the monthly mean from the NoENSO. ....	44
Figure 4.1	DJF Interannual sea surface temperature (SST) Variance. Top: Interannual variance from the CTRL run. Bottom: Interannual variance from the NoENSO run. Intervals of contours are 0.2 (°C) <sup>2</sup> . ....	51
Figure 4.2	DJF SST Percent Difference of Interannual Variance. Red shading: ENSO increases variability. Blue shading: ENSO displaces variability. Grey shading: Insignificant values based on a 95% confidence level. Intervals of contours are 10%.....	52
Figure 4.3	DJF Interannual 500 hPa geopotential height (Z500) Variance. Top: Interannual variance from the CTRL run. Bottom: Interannual variance from the NoENSO run. Intervals of contours are 500 <i>meters</i> <sup>2</sup> . ....	53
Figure 4.4	CESM1-CAM4 DJF Z500 Percent Difference of Interannual Variance, comparing ENSO and NoENSO. Red shading: ENSO increases variability. Blue shading: ENSO displaces variability. Intervals of contours are 10%. Grey shading: Insignificant values based on a 95% confidence level.....	54
Figure 4.5	DJF Interannual 200 hPa zonal wind (U200) Variance. Top: Interannual variance from the CTRL run. Bottom: Interannual variance from the NoENSO run. Intervals of contours are 5 ( <i>m/s</i> ) <sup>2</sup> .....	55
Figure 4.6	DJF U200 Percent Difference of Interannual Variance. Red shading: ENSO increases variability. Blue shading: ENSO displaces variability. Intervals of contours are 10%. Grey shading: Insignificant values based on a 95% confidence level.....	56
Figure 4.7	DJF Precipitation Percent Difference of Interannual Variance. Red shading: ENSO increases variability. Blue shading: ENSO displaces variability. Intervals of contours are 10%. Grey shading: Insignificant values based on a 99% confidence level, and 100 ( <i>mm/month</i> ) <sup>2</sup> has been masked in the CTRL	

run.....	57
Figure 4.8 DJF Precipitation Percent Difference of Interannual Variance over North America. Red shading: ENSO increases variability. Blue shading: ENSO displaces variability. Intervals of contours are 10%. Insignificant values have been removed based on a 99% confidence level, and 100 ( <i>mm/month</i> ) <sup>2</sup> has been masked in the CTRL run.....	58
Figure 4.9 DJF Interannual Precipitation Variance. North American Interannual variance from the CTRL run. Intervals of contours are 200 ( <i>mm/month</i> ) <sup>2</sup> . Mask has been applied over the ocean. Precipitation Variance has been normalized based on CTRL climatological precipitation.....	59
Figure 5.1 NCEP/NCAR reanalysis DJF Z500 percent difference of interannual variance (1950-2020). Comparison between ENSO and neutral events based on a Nino3.4 ENSO threshold of $\pm 0.5^{\circ}\text{C}$ . Red shading: ENSO increases variability. Blue shading: ENSO displaces variability. Intervals of contours are 10%. Grey shading: Insignificant values based on a 90% confidence level.....	70
Figure 5.2 CESM1-CAM4 DJF Z500 percent difference of interannual variance. Comparison between CTRL ENSO and Neutral events based on a Nino3.4 ENSO threshold of $\pm 0.5^{\circ}\text{C}$ . Red shading: ENSO increases variability. Blue shading: ENSO displaces variability. Intervals of contours are 10%. Grey shading: Insignificant values based on a 90% confidence level.....	71
Figure 5.3 CESM1-CAM4 DJF Z500 percent difference of interannual variance. Comparison between CTRL ENSO and Neutral events based on a Nino3.4 ENSO threshold of $\pm 0.17^{\circ}\text{C}$ , from the NoENSO Nino3.4 standard deviation. Red shading: ENSO increases variability. Blue shading: ENSO displaces variability. Intervals of contours are 10%. Grey shading: Insignificant values based on a 90% confidence level.....	72
Figure 5.4 CESM1_CAM4 DJF Z500 percent difference of interannual variance, comparing ENSO and 40 random 40 NoENSO DJF years. Red shading: ENSO increases variability. Blue shading: ENSO displaces variability. Intervals of contours are 10%. Grey shading: Insignificant values based on a 95% confidence level. ....	73
Figure 5.5 Z500 DJF Percent change of average variance over (43°N-47°N,105°W-95°W). Blue dots are the percent change based on the average NoENSO variance, based on 10000 random samples of a specific sample size. Error bars are the percent uncertainty derived from the standard deviation of individual sample of NoENSO variance. The x-axis is sample sizes of DJF ENSO neutral years. The y-axis is percent change listed as a percentage. ....	74
Figure 5.6 Z500 DJF Percent change of average variance over (27°N-33°N,105°W-95°W).	

Red dots are the percent change based on the average NoENSO variance, based on 10000 random samples of a specified sample size. Error bars are percent uncertainty derived from the standard deviation of individual sample of NoENSO variance. The x-axis is sample sizes of DJF ENSO neutral years. The y-axis is percent change listed as a percentage. .... 74

Figure 5.7 CESM2 DJF Z500 percent difference of interannual variance. Comparison between CTRL ENSO and Neutral events based on a Nino3.4 ENSO threshold of  $\pm 0.17^{\circ}\text{C}$ , from the NoENSO Nino3.4 standard deviation. Red shading: ENSO increases variability. Blue shading: ENSO displaces variability. Intervals of contours are 10%. Grey shading: Insignificant values based on a 90% confidence level. .... 75

# 1 Introduction

## 1.1 What is ENSO?

The El Niño-Southern Oscillation (ENSO) is characterized by the fluctuation of sea surface temperatures (SST) between warm El Niño events and cold La Niña events in the equatorial eastern and central Pacific Ocean. The maximum ENSO-related anomalous SST occurs in the boreal winter, although ENSO onset can occur as early as the previous spring. ENSO is the dominant source of interannual variability in the tropical ocean-atmosphere system and operates on a 2-7-year period with individual ENSO events lasting 1-2 years.

Fluctuations of SST in the equatorial Pacific impact large-scale atmospheric circulation through anomalous deep convection and latent heat release in the equatorial Indo-Pacific Ocean (Hoskins and Karoly, 1981). The shift in large-scale atmospheric circulation, due to ENSO, can alter the associated global weather patterns (Ropelewski and Halpert, 1987). Changes in weather patterns can enhance the risk of natural disasters, such as droughts, heavy rainfall, floods, and heat waves (Dilley and Heyman, 1995). These terrestrial impacts can influence the severity of ecological and economical disasters, such as the destruction of fisheries, low crop yield, and water scarcity (McPhaden et al., 2006). For example, the El Niño event of 1982-1983 was one of the strongest ENSO events on record and caused an estimated \$13 billion in economic loss and property damage. Floods, droughts, and wildfires were the cause of the majority of the destruction (Golnaraghi and Kaul, 1995). Societies that are most vulnerable to ENSO, particularly those most reliant on agricultural and hydrological resources, are dependent on continued scientific progress to increase ENSO prediction skill.

The growth mechanism that supports an ENSO event is referred to as the Bjerknes feedback (Bjerknes, 1969). The Bjerknes Feedback is a positive atmosphere-ocean feedback loop

that reinforces an initial SST anomaly. As stated above, during an El Niño event, SST are anomalously warmer in the eastern Equatorial Pacific and cooler in the western Equatorial Pacific. These changes in the surface temperature weaken the zonal SST gradient and as a result, weaken the zonal pressure gradient that dictates the strength of the Walker circulation. A weaker pressure gradient reduces the strength of the trade winds along the equator, reducing upwelling in the eastern equatorial Pacific and downwelling in the western equatorial Pacific. A reduction in upwelling and downwelling reinforces the initial warm SST anomaly in the eastern equatorial Pacific and cold SST anomaly in the west. Over time, the initial warm SST anomaly can amplify into a mature El Niño event.

For a La Niña event, the same Bjerknes positive feedback loop occurs but with an opposite sign initial SST anomaly. Cold SST anomalies are present in the eastern equatorial Pacific and warmer SST in the western equatorial Pacific. The zonal SST and pressure gradient strengthen, enhancing the strength of the easterlies and Walker Circulation. Stronger easterlies increase downwelling in the western equatorial Pacific and upwelling in the eastern equatorial Pacific, further enhancing the zonal SST gradient. What begins as a weak cooling in the east matures into a full-fledged La Niña event.

The Bjerknes Feedback requires an initial perturbation to kick-start the feedback loop. In the Bjerknes Feedback explanation given above, an initial SST anomaly was the main factor in the onset of an ENSO event. In this scenario, the SST anomaly forces a change in the overlying atmosphere and in return the atmospheric perturbation dynamically forces the ocean. However, the Bjerknes feedback can be initiated through atmospheric forcings as well. Atmospheric wind variability can dynamically force the ocean, in the form of wind stress, along the equatorial Pacific (e.g., Lau et al, 1989 Moore and Kleeman, 1999; Gebbie et al., 2007; Seiki and

Takayabu, 2007). This anomalous wind stress can excite free long oceanic wave propagation, like the equatorial Kelvin and Rossby waves (Pedlosky, 2004). The equatorial Kelvin wave is centered along the equator and propagates eastward. The initial Kelvin wave carries either warming or cooling anomalies along the equatorial thermocline that eventually emerge at the surface in the eastern equatorial Pacific (Battisti and Hirst, 1989, Suarez and Schopf, 1988). If the SST anomalies are large enough in magnitude, they may ignite the Bjerknes feedback. Whether the Kelvin wave generates a warm or cold SST anomaly depends on the sign of the initial wind stress anomaly.

## **1.2 ENSO Impacts on the Overlying Atmosphere**

Understanding the overlying atmospheric circulation in the tropical Pacific is important because of the major role ENSO plays in modifying its relative strength and position. The two largest global overturning atmospheric circulations are the Hadley and Walker Circulations (Schwendike et al., 2015). The purpose of global atmospheric circulation is to redistribute heat. The Hadley Circulation is a dominantly meridional circulation that brings warm air away from the equator towards the poles and cold air from higher latitudes towards the equator. Warm air ascends at the equator and moves aloft towards the poles in the upper troposphere. As the warm air moves to higher latitudes the air cools and descends. Cool air from higher latitudes travels towards the equator, along the surface, where it warms and ascends at the equator. The zonal atmospheric circulation along the equator that occurs between the northern and southern Hadley Circulation cells is called the Walker Circulation (Bjerknes, 1969).

Typically, due to the climatological easterlies along the equator, warm water is pushed to the western boundary of the Equatorial Pacific; this region is referred to as the Pacific warm

pool. At the same time, the overlying easterlies force deeper ocean water to upwell towards the surface in the eastern Pacific. Upwelling in the eastern Pacific results in relatively cooler temperatures in the east compared to the west. On average, warm air rises in the western equatorial Pacific, creating regions of deep convection. The air mass then travels to the east in the upper troposphere, parallel to the equator, and sinks over the eastern equatorial Pacific over the region with cooler SST. The falling air is picked up by the easterly trade winds and transported to the west where the circulation continues. This circulation pattern is the typical Walker Circulation associated with the ENSO neutral state.

When ENSO is present, the Walker Circulation is shifted because the locations of rising and falling air depend on the location of the relatively warm and cool SST. This shift directly influences the location of rising and falling air along the tropical Pacific, which impacts the main regions of convection and changes the regional climate on interannual timescales. Severe societal and economical impacts can occur in countries found along the equatorial Pacific. During an El Niño event, when it is anomalously warmer in the eastern equatorial Pacific and cooler in the western equatorial Pacific, the main convective region is shifted to the east. This shift leaves Australia and Indonesia more susceptible to droughts, while off the northwest coast of South America severe flooding and warmer ocean temperatures can occur. During a La Niña event, the Walker Circulation shifts further west and intensifies. Cooler than average SST are found in the eastern equatorial Pacific, and due to the increased strength of the Walker Circulation, warmer SST are concentrated to the far western region of the equatorial Pacific. The main convective region is formed in this region, which causes increased risk of flooding over Australia and Indonesia; and droughts and cooler than average temperatures on the northwest coast of South America. Due to these impacts, amongst others, developing climate and forecast models to better

simulate and predict ENSO and ENSO's teleconnections has been the focus of decades of research.

### **1.3 ENSO Impacts on the Extra-tropics**

The connections between local ENSO forcing in the equatorial Pacific and the various global climatic impacts in the extra-tropics are often referred to as ENSO teleconnections and can be explained by tropical and extratropical atmospheric dynamics (Gill, 1980; Hoskins and Karoly, 1981). In the Northern Hemisphere, the ENSO teleconnection pattern is strongest during the boreal winter, when ENSO is at peak amplitude (Ropelewski and Halpert, 1986). During an El Niño event, the displacement of the Walker Circulation produces anomalous heating in the central equatorial Pacific through anomalous deep convection and latent heat release. This anomalous heating forces anomalous upper-level divergence in the tropics and intensifies the Hadley Circulation (Trenberth et al., 1998). Through the intensification of the Hadley Circulation and subsequent changes to the Northern Hemisphere subtropical jet, a stationary Rossby wave train pattern is generated from the tropical Pacific into the midlatitudes (Hoskins and Karoly, 1981). The Rossby wave train pattern is more evident during periods when the midlatitude westerlies are the strongest, specifically the boreal winter (Hoskins and Ambrizzi, 1993).

The Northern Hemisphere Rossby wave train projects onto what is referred to as the Pacific North American (PNA) Pattern (Wallace and Gutzler, 1981). Put simply, the PNA is the resulting spatial pattern of atmospheric variability associated with changes in the Pacific jet (Hoerling et al., 1997). ENSO strongly dictates the strength and location of the North Pacific jet. The positive phase of the PNA often occurs during the positive phase of ENSO. During El Niño,

lower than average 500 hPa geopotential heights occur in the vicinity of the Aleutian low and across the southeastern United States with higher-than-average heights over the northwest United States into Canada and in the north-central Pacific. A negative PNA pattern, with a pattern opposite in sign to the positive phase, is oftentimes associated with a La Niña event (Hoerling and Kumar, 2002).

ENSO forced changes in the atmospheric circulation can have terrestrial impacts including precipitation and surface temperature (Harrison and Larkin, 1998; Ropelewski and Halpert, 1987). For example, ENSO can be felt across the globe through variation in precipitation patterns. The impact of ENSO on the seasonal precipitation pattern over the United States and occasionally all North America is the focus of many previous studies (Ropelewski and Halpert, 1986; Kiladis and Diaz, 1989; Trenberth et al., 1998; Chen et al., 2017; L'Heureux et al., 2015; Deser et al., 2018). Based on observational findings, during an El Niño event, wetter than average conditions are found across the southern region of the United States and northern Mexico. The northwestern and northeastern regions of the United States typically experience drier than average conditions. The opposite sign spatial pattern is observed during a La Niña year with wetter conditions in the northwest and northeast United States and drier conditions across the southern United States. However, not every El Niño or La Niña event results in these canonical patterns due to abundant natural variability and other large-scale patterns that can impact North American precipitation (L'Heureux et al., 2017).

#### **1.4 Quantifying ENSO's Impacts on Climate Variability**

In previous studies, investigating ENSO and ENSO's impacts have been done through various statistical analyses. Some common methods as explained by Compo and Sardeshmukh

(2010) include regression analysis, applying a filter over low frequency signal, assuming all variability in the Nino3.4 region is driven by ENSO, and the assumption that all ENSO variability is explained by the First Principal Component. However, these methods contain caveats, such as ENSO contains nonlinearities (Frauen et al. 2014), some studies show that ENSO contains a low frequency signal (Wittenberg 2014), the Nino3.4 region can be influenced by non-ENSO variability including tropical instability waves (Tian et al. 2019) and thermally coupled modes (Larson et al. 2018), and ENSO can have a lagged atmospheric response (Su et al. 2005). For these reasons, the removal of ENSO through statistical analysis may not fully remove ENSO or may remove other natural variability unrelated to ENSO.

In reality, the observational record is limited and the impacts from one El Niño or La Niña event can be vastly different from the next due to differences in the SST anomaly spatial patterns (Capotondi et al., 2015). Furthermore, other non-ENSO variability can overwhelm the ENSO forced variability. For this reason, climate model simulations are often used, along with observational data, to evaluate ENSO and ENSO teleconnections. More recently, studies have attempted to remove ENSO by dynamically suppressing the Bjerknes feedback in coupled models (Larson and Kirtman 2015, Larson et al. 2018). When using this method, the ocean is unable to respond to the anomalous wind variability produced by the atmosphere over the equatorial Pacific Ocean. By doing this, an initial SST anomaly is unable to develop into an ENSO event. In this study, this method is used to conduct an experiment without ENSO variability. This experiment will then be compared with an experiment that has all of Earth's circulations fully represented.

Due to large variability associated with both El Niño and La Niña events and their teleconnections, multi-century model simulations are needed to determine the robustness of

ENSO forced variability. When comparing El Niño and La Niña events to the typical neutral conditions, not only is a large sample of El Niño and La Niña events needed, but a large sample of ENSO neutral events are needed as well. This is because non-ENSO variability has proven to be significant (Deser et al., 2012). Previous studies suggest that a minimum record length of 250 years is needed to confidently assess ENSO and ENSO teleconnections (Stevenson et al. 2010). This idea will be investigated later in this study.

The purpose of this study is to investigate the ENSO-driven impacts on interannual atmospheric circulation variability through the comparison of novel climate model experiments. The observational and model datasets used are discussed in the following section. The model experiments are described and validated in section 3. Section 4 shows the results found from the model experiment comparison. In Section 5, the model simulation length required to resolve ENSO and ENSO teleconnections will be addressed in section 5. A summary and conclusion are stated in section 6.

## 2 Data and Analysis Methods

### 2.1 Observational Datasets

The sea surface temperature (SST) dataset used is the Extended Reconstructed Sea Surface Temperature version 5 (ERSST.v5; Huang et al. 2017). The horizontal grid spacing of the ERSST.v5 is  $2^\circ \times 2^\circ$  and missing data are interpolated for spatial completeness. The International Comprehensive Ocean-Atmosphere Dataset (ICOADS) is used as the input dataset to create the global monthly ERSST.v5 Reanalysis Dataset. The latest version of ERSST.v5 uses the ICOADS version 3, which uses SST from Argo floats and Hadley Centre Ice-SST version 2 ice concentration. In order to compare the mean state of observations with the model, which uses constant present day forcing representative of the year 2000, data from 1980-2020 is used. However, all other calculations use the full time series from 1950 to the end of 2020, such as ENSO composite anomalies and interannual variance. The SST data is available from 1854, however data collected following the 1940s is more reliable (Huang et al., 2017).

Atmospheric variables zonal and meridional 200 hPa wind (U200 and V200, respectively), 500 hPa geopotential height (Z500) are from the National Centers for Environmental Prediction (NCEP)–National Center for Atmospheric Research (NCAR) reanalysis project (hereafter, NCEP/NCAR reanalysis; Kalnay et al., 1996). The NCEP/NCAR reanalysis dataset is available from 1948 to the present day on a  $2.5^\circ \times 2.5^\circ$  grid. The Precipitation data is from the NOAA Precipitation Reconstruction (PREC; Chen et al., 2002) in millimeters per day. This dataset has the same grid spacing as the NCEP/NCAR dataset. Data from 1948 is available in the PREC dataset. Data from 1950 to present is used for both atmospheric datasets, NCEP/NCAR reanalysis and PREC, to align with the ERSST.v5 data used.

## 2.2 Model Description and Validation

Two coupled models are used in this analysis. The first model, the Community Earth System Model version 1 with the Community Atmospheric Model version 4 (CESM1-CAM4, Worley et al., 2011), is used for two experiments. The control experiment (CTRL) is the first experiment discussed below. The CTRL experiment simulates Earth's climate system and resolves ENSO variability. This experiment will be compared with observations to validate the model's ability to simulate Earth's climate and ENSO teleconnections. Following the validation of the CTRL experiment, the second CESM1-CAM4 experiment will be introduced. In the second model experiment (NoENSO), ENSO variability has been eliminated through the suppression of the dynamical processes that support ENSO variability. Next, the two experiments, CTRL and NoENSO, will be compared through a series of statistical analyses. This is done to assess the impact the removal of ENSO variability has on the mean state, Nino3.4 region and interannual variability over North America. Then, we explore how sampling variability impacts how ENSO and ENSO teleconnections are resolved in observations and CESM1-CAM4. Finally, a second model, the Community Earth System Model version 2 (CESM2, Danabasoglu et al., 2020), is used to test the hypotheses generated from the model experiment comparison. CESM2 is chosen due to the long simulation length and the model's ability to accurately simulate the spatial pattern of ENSO teleconnections (Capotondi et al. 2020).

## **2.2.1 Community Earth System Model Version 1 – Community Atmospheric Model**

### **Version 4**

The NCAR CESM1-CAM4 state-of-the-art climate model is used in this study due to its ability to simulate ENSO and ENSO teleconnections (Deser et al. 2012). The data used in this study is simulated using the base code of the CESM1 while using the same model components as found in the CCSM4 version. The CESM1-CAM4 has a horizontal grid spacing of  $1^\circ \times 1^\circ$ . The CESM1-CAM4 is similar to the CCSM4, however it allows for a wider range of capabilities. These capabilities include interactive carbon-nitrogen cycling, global dynamic vegetation, land use changes, marine biogeochemistry, and a dynamic ice sheet model (Hurrell et al., 2013). CESM1-CAM4 uses a flux coupler to concurrently simulate Earth's climate system using four separate models: ocean, atmosphere, land, and sea-ice. The role of the flux coupler is to exchange mean-state information and fluxes between the different components. A new spin-up procedure, a procedure used to statistically stabilize and reach a model's climatology, used in the CESM1-CAM4 reduces biases in sea surface temperature and surface salinity in the ocean model. (Danabasoglu et al. 2012).

A present-day configuration is used for both experiments. The model is forced throughout the simulation with a constant atmospheric composition from the year 2000. This has been done to appropriately represent the current sea-ice extent in the higher latitudes. By using set aerosol and greenhouse gas atmospheric composition, the data is not influenced by anthropogenic trends and climate variability cannot be explained by changes in external forcing. This was done to simulate the present-day earth climate system similar to what is found in recent observational data (Gent et al., 2011).

The Parallel Ocean Program version 2 (POP2; Danabasoglu et al. 2012) is the ocean component in CESM1-CAM4. The model has 60 vertical levels largely concentrated in the upper ocean with a 10-meter resolution in the top 160 meters. Physical changes to the equatorial current structure, slope of the thermocline, and removal of the cold bias in the equatorial cold tongue improved the biases found in the Pacific Ocean.

The Community Atmospheric Model version 4 (CAM4; Neale et al. 2013) is used as the atmospheric component in CESM1-CAM4. For this reason, CESM1-CAM4 compares closely to CCSM4, as the out-of-the-box version of CESM1 typically uses the updated CAM5. The CAM4 has a dynamical core, which allows for better transport and conservation properties (Neale et al. 2010). Hadley Circulation parameterizations have reduced biases in annual mean, tropical easterly, subtropical westerly, and the southern hemisphere mid-latitude jet during boreal winter. (Neale et al., 2013) (Gent et al, 2011). These changes have resulted in improved phase, amplitude, and anomalous spatial pattern of ENSO simulations (Neale et al., 2008).

The Community Land Model version 4 (CLM4; Lawrence et al. 2011; Oleson et al. 2010) is the land model used in the CESM1-CAM4. The Community Ice Code version 4 (CICE4, Holland et al., 2012) is the sea-ice model in the CESM1-CAM4. This model contains two main components, dynamics, involving the movement of sea-ice, and thermodynamics, involving the vertical temperature profile of the ice, spatial growth, both vertically and laterally, and the rate of melting. (Holland et al., 2012).

This model will be used to perform two model experiments to assess ENSO's interannual impacts on global atmospheric circulation variability, as well as precipitation and surface temperature variability over North America.

### 2.2.2 Community Earth System Model Version 2

The Community Earth System Model version 2 (CESM2; Danabasoglu et al., 2020) is the latest version of the earth system model produced by NCAR. Similar to CESM1-CAM4, the horizontal grid spacing of CESM2 is approximately  $1^\circ \times 1^\circ$ . CESM2 consists of fully interactive ocean, land, sea-ice, land-ice, river, wave, and atmospheric models. The atmospheric model is the Community Atmospheric Model version 6 (CAM6, Bogenschutz et al., 2018) with 32 vertical levels. The introduction of the unified turbulent scheme called Cloud Layers Unified by Binormals (CLUBB) improves cloud and precipitation biases in the model. CESM2 uses the same model, (POP2, Danabasoglu et al., 2020), for the ocean component as used in the CESM1-CAM4. However, POP2 has been updated since CESM1, such as the introduction of the wave component, the NOAA WaveWatch-III ocean surface wave prediction, with  $4^\circ$  longitude by  $3.25^\circ$  latitude grid spacing. The Community Ice Code version 5 (CICE5, Hunke et al., 2015) is the ice component and the Community Land Model Version 5 (CLM5, Lawrence et al., 2019) is the land component used in the CESM2 with the similar horizontal grids as the ocean and atmosphere components respectively (Danabasoglu et al. 2020).

Although CESM1-CAM4 is used for the model experiments, CESM2 is used to test the hypotheses that are formulated from the comparison of the CTRL and NoENSO analyses. In particular, CESM2 is useful because of the long simulation length, approximately 2000 years, and the model's ability to represent global ENSO teleconnections, both in spatial pattern and seasonality (Capotondi et al. 2020). Limitations exist in this version of the model, some of which being a 30% overestimation of ENSO's amplitude, based on the standard deviation of the monthly Nino3.4 index, as well as slight differences in the zonal extent of anomalous SST along the equatorial Pacific.

### 2.3 Analysis Methods

To compare observations with output from the two models, CESM1-CAM4 and CESM2, all observational and reanalysis datasets are linearly detrended to approximately remove the presence of anthropogenic trends. Generally, monthly anomalies are calculated by removing the respective monthly mean climatology of each experiment. After calculating the monthly anomalies, the seasonal averages are calculated using a three-month moving average method. This method takes the average of three sequential monthly anomalies, which smoothes the data and produces seasonal averages. In this study, the boreal winter seasonal average (DJF) is used because the largest ENSO related anomalies in the equatorial Pacific and the most robust global teleconnective response to ENSO occurs in these months (Deser et al. 2012). To calculate the Nino3.4 index, the DJF seasonal anomalies in the equatorial Pacific are area-weighted and averaged over the Nino3.4 region from 5°N-5°S, 120°-170°W. To categorize ENSO events, a threshold of  $\pm 0.5^{\circ}\text{C}$  is set, based on Climate Prediction Center (CPC) guidelines. An El Niño event is defined as when the DJF Nino3.4 meets or exceeds  $0.5^{\circ}\text{C}$ , whereas a La Niña event is defined when the DJF Nino3.4 is less than or equal to  $-0.5^{\circ}\text{C}$ .

The interannual variance is calculated using the DJF seasonal anomalies; this is done to show the amount of variability present from year-to-year during the boreal winter. Interannual variance is calculated for both the CTRL and NoENSO experiments. To quantitatively and visually compare each experiment's interannual variability, the following percent difference equation (1) is applied to a variety of ocean and atmospheric variables,

$$\text{Percent Difference} = \left( \frac{\sigma_{CTRL}^2 - \sigma_{NoENSO}^2}{\sigma_{NoENSO}^2} \right) * 100, \quad (1)$$

where  $\sigma_{CTRL}^2$  is the DJF interannual variance of the CTRL experiment and  $\sigma_{NoENSO}^2$  is the DJF interannual variance of the NoENSO experiment. The percent difference equation is used throughout this study to investigate ENSO's forced response.

In observations, the percent difference equation is defined as the following,

$$Percent\ Difference = \left( \frac{\sigma_{CTRL}^2 - \sigma_{Neutral}^2}{\sigma_{Neutral}^2} \right) * 100, \quad (2)$$

where  $\sigma_{Neutral}^2$  is the variance of the ENSO neutral events based on the provided Nino3.4 threshold. This percent difference equation differs from the equation used to compare the two experiments in the neutral atmospheric conditions used. In the experimental comparison, the NoENSO experiment contains a very neutral Equatorial Pacific state. However, this NoENSO state is not possible to obtain in observations, so the previously defined ENSO-neutral state is used for an apples-to-apples comparison.

An F-test is used to determine the statistically significant regions in the percent difference plots for all variables. The total number of independent samples is calculated using the effective degrees of freedom; this method uses an autocorrelation function to take into account the wintertime climate anomalies that correlate from year to year. This is done at each grid point. If a lagged correlation exists and is significant based on a 95% confidence level, meaning that the climate anomaly at lag-0 is significantly correlated to the climate anomaly at lag-N, then the total sample size is reduced using the estimated effective degrees of freedom.

## **3 Model Experiments and Validation**

### **3.1 CTRL Experiment**

In this section, we compare the 322-year simulation of the Pacific mean state, ENSO variability, and ENSO teleconnections in the CTRL experiment with observations and reanalysis products. We also compare the CTRL experiment with the NoENSO experiment to assess the impacts of ENSO on global climate variability.

#### **3.1.1 Mean State Comparison to Observations**

The DJF seasonal climatology of SST, Z500, and U200 in CESM1-CAM4 CTRL and observations are compared to assess the usefulness of the model for further analyses. The mean state of the equatorial Pacific strongly influences key ENSO characteristics, such as amplitude and periodicity (Fedorov and Philander, 2000).

Figure 3.1 shows the DJF climatology for SST in CESM1-CAM4 and observations. In both the model and observations, SSTs are latitudinally dependent with warmer temperatures in the lower latitudes and cooler temperatures towards the poles, as expected. The strongest meridional SST gradient occurs in the mid-latitudes. The SSTs are relatively uniform across the equatorial region apart from slightly cooler temperatures in the eastern region of the Equatorial Pacific, indicative of the cold tongue. The model overestimates the climatological SST in the western equatorial Pacific, as well as along the coastal region of the southeastern Equatorial Pacific, with cooler than expected temperature to the north of this region, off the west coast of Central America. Figure 3.2 shows the zonal SST seasonal climatology for the CESM1-CAM4

and the ERSTT.v5. The CESM1-CAM4 overestimates the mean SST for all seasons. The DJF seasonal climatology is overestimated by approximately 1°C across the entire equatorial Pacific.

The mid-level atmospheric geopotential height at 500 hPa, Z500, is also analyzed because it generally represents the steering flow of the atmosphere and can be used to connect what is occurring at higher levels and the surface. The DJF Z500 climatology is shown in Figure 3.3 for both the CTRL experiment and observations. Typical features of geopotential heights at 500 hPa are higher uniform heights across the entire tropical region, a steep gradient in the midlatitudes, and lower heights at the poles. Through visual comparison, relatively higher heights extend further north in the midlatitudes in the model compared to observations. Higher heights are also seen in certain regions of the tropics and extra-tropics than what is observed. Higher heights in the tropics are to be expected due to warmer SSTs in the CESM1-CAM4 equatorial Pacific.

The U200 is compared in the CESM1-CAM4 because ENSO is known to shift the position of the jet stream. These changes in the speed and location of the Pacific jet stream, which extends over North America, relocates weather systems, altering the regional climate (Reiter and Bierly, 2005). When comparing the CESM1-CAM4 U200 climatology to observations in Figure 3.4, the spatial pattern is well replicated, with a strong Pacific jet in the Northern Hemisphere, a relatively weaker jet in the Southern Hemisphere, and trade winds along the equator. The meridional tropospheric temperature gradient is stronger in the Northern Hemisphere during boreal winter, producing a stronger jet stream during these months. However, the CESM1-CAM4 overestimates the strength of the zonal jet compared to what is observed in nature, and the zonal extent of the Pacific jet stretches further across the North

Pacific basin than what is observed in nature. Overall, the model produces realistic climatology compared with observations in SST, Z500, and U200, as also concluded in Gent et al. (2011).

### **3.1.2 ENSO Variability Comparison to Observations**

A climate model's ability to simulate ENSO and ENSO teleconnections accurately is crucial in understanding the global impacts of ENSO. A 300-year long control integration of the CESM1-CAM4 allows for a more thorough investigation of ENSO characteristics and statistics, such as El Niño- La Niña amplitude asymmetries and ENSO's global atmospheric teleconnections (Deser et al. 2012, hereafter referred to as D12). The Nino3.4 index is used to assess the ENSO variability and periodicity. This region is selected because it best represents SST variability associated with the ENSO state (Barnston et al. 1997). Figure 3.5 shows roughly 40 years of the monthly Nino3.4 time series from the CTRL along with the ERSST.v5 observational record from 1980-2020. Compared to observations, the CTRL simulates higher amplitude ENSO events, especially La Niña events. ENSO variability in observations is highly irregular, with fluctuations in duration of events and periodicity. In the model, ENSO variability fluctuates from cold to warm events at a more periodic rate than what is seen in nature; these findings are consistent with D12.

Next, several calculations are performed to compare the statistics of ENSO variability in the model and observations. The amplitude of the Nino3.4 variability is assessed using the standard deviation of the full monthly time series in both the CTRL and observations. The standard deviation of the Nino3.4 index in observations is  $0.87^{\circ}\text{C}$ , whereas the standard deviation in the CTRL is  $0.99^{\circ}\text{C}$ . Consistent with D12, Nino3.4 variability in the CESM1-CAM4 overestimates that in nature. An autocorrelation calculation is used to quantitatively compare the

typical duration of Nino3.4 SST anomalies and determine if the ENSO cycle in the model is oscillatory (Figure 3.6). Given that the CTRL autocorrelation shows regular fluctuations from positive and negative correlations, it is clear that the model oscillates between El Niño and La Niña events more periodically than what is found in nature. Observations show that there is smaller correlation from one event to another, suggesting that in nature, individual ENSO events are not always as connected to the prior ENSO event as in the CTRL.

To compare the dominant timescales of ENSO variability in the model and observations, a power spectral density analysis is applied to the Nino3.4 indices (Figure 3.7). The dominant spectral peak in the CTRL is between 3-6 years with a maximum power occurring at 4 years. This is larger and less variable than what is found in observations, consistent with D12 and Gent et al. (2011). The spectral peaks found in the ERSST.v5 are between 3-8 years, showing that ENSO does not operate on a fixed periodicity but occurs on a variety of interannual timescales. Additionally, differences exist between the magnitude of power in the CTRL and ERSST.v5 are also shown at decadal time scales. More variability is found in nature at longer timescales than what is represented in the CTRL.

The SST anomalies associated with ENSO events force an atmospheric response, altering the global circulation patterns. To investigate these patterns in the CTRL and observations, ENSO composite anomalies are calculated over DJF. In observations, 22 El Niño events and 22 La Niña events are used in the analysis. In the CTRL, 100 El Niño and 100 La Niña events are used. Figure 3.8 shows the DJF ENSO composite anomalies for SST, with El Niño composites for observations and CTRL shown in Figure 3.8(a,c) , respectively, and La Niña composites for observations and CTRL shown in Figure 3.8(b,d), respectively. A few familiar features of El Niño anomalies are evident. Both the CTRL and observations show warmer than average SST

anomalies in the eastern equatorial Pacific with cooler than average SST in the western equatorial Pacific. Comparing the El Niño composites reveals that the CTRL underestimates the off-equatorial spread of the warm SST anomaly, which may be attributed to the differences in ENSO-related variability found on decadal time scales. Additionally, the CTRL overestimates the amplitude of El Niño anomalies, which could influence the strength of El Niño teleconnections. The zonal extent of the warm SST anomaly in the eastern equatorial Pacific stretches too far west into the warm pool region, which creates a warm pool bias in the CESM1-CAM4, consistent with D12.

The expected extratropical SST anomalies associated with ENSO events are also apparent. Warmer than average SST in the tropical Pacific ultimately impacts the midlatitudes through an atmospheric Rossby wave train. Atmospheric Rossby waves alter the atmospheric forcing on the ocean, which drive extratropical SST anomalies through a process referred to as the atmospheric bridge (Alexander et al., 2002). During an El Niño event, cooler than average SST are found within the North Pacific subtropical gyre and warmer than average SST are found along the associated boundary currents.

La Niña SST composite anomalies show a similar but opposite sign spatial pattern with cooler than average anomalies in the eastern equatorial Pacific and slightly warmer SST anomalies in the warm pool region Figure 3.8(b). When comparing observations and the CTRL La Niña anomalies, the zonal extent of the anomalously cool SSTs extend too far west into the warm pool region, similar to what occurs in the model's El Niño anomalies. The model underestimates the SST variability occurring in the extratropical and midlatitude regions. These differences agree with conclusions in D12. Although not shown here, the typical duration of ENSO events is well reproduced in the CTRL (D12).

The Z500 composite anomalies, Figure 3.9, and U200 composite anomalies, Figure 3.10, are shown to assess how well the CTRL experiment simulates ENSO related circulation anomalies in the middle and upper levels of the atmosphere. During El Niño events, anomalously high Z500 are found across the entire equatorial region in both the CTRL Figure 3.9(a) and observations Figure 3.9(c). Anomalously low Z500 are found in the vicinity of the Aleutian Low and extend into the southeastern United States, and anomalously high Z500 are present over the far Northern region of North America. This pattern is consistent with part of the PNA pattern. The CTRL experiment overestimates the amplitude of the Z500 anomalies found in nature, however the model accurately simulates the overall spatial pattern, specifically the location of the anomalous dipole in the Northern Pacific (Deser et al 2012).

At 200 hPa, during an El Niño event, the climatological easterly winds are weakened in the equatorial region while the climatological westerly winds in the midlatitudes are strengthened, particularly in the Northern Hemisphere when the Rossby wave formation is strongest during the boreal winter Figure 3.10(a). In addition to the Rossby wave formation, which influences ENSO teleconnections, the eddy-driven mean meridional circulation drives hemispherically symmetric variability and projects onto the zonal mean during ENSO events (Seager et al., 2003). A similar anomalous spatial pattern is found during La Niña events, however the easterlies are strengthened across the equatorial Pacific and the westerlies are weakened in both Hemispheres Figure 3.10(b). The model overestimates the strength of the anomalous winds in the midlatitudes, particularly in the Northern Hemisphere, likely due to the higher ENSO amplitude in the model. Overall, the spatial pattern of ENSO-driven anomalous winds is well represented in the CTRL.

## **3.2 NoENSO Experiment**

In this study, a novel approach to the removal of ENSO in CESM1-CAM4 is used to investigate the atmospheric impacts of ENSO. In this experiment, referred to as the NoENSO experiment, ENSO variability has been removed through damping the physical process that supports ENSO variability, known as the Bjerknes Feedback (Bjerknes, 1969). As previously mentioned, the Bjerknes feedback is a positive feedback loop between the ocean and the atmosphere that reinforces an initial SST anomaly in the equatorial Pacific. For example, suppose an initial weak warm SST anomaly is present in the equatorial eastern Pacific. This warm SST anomaly weakens the climatological zonal SST gradient across the Pacific, which then weakens the easterly trade winds that are part of the Walker Circulation. The weakened trade winds reduce the climatological upwelling and downwelling along the equatorial Pacific, resulting in a strengthening of the initial warm SST anomaly in the east, further weakening the zonal SST gradient. This positive feedback essentially allows the warm SST anomaly to grow in a mature El Niño event. When the Bjerknes feedback is disabled, say by decoupling the wind anomalies from the SST (described below), ENSO events are unable to develop. How the Bjerknes feedback is deactivated in the model is described below.

### **3.2.1 Experimental Design**

The NoENSO experiment is performed using the same CESM1-CAM4 base model as the CTRL experiment. However, NoENSO uses a methodology introduced in Larson and Kirtman (2015), where a mechanically decoupled configuration is applied to the tropical Pacific Ocean grid points, which allows the wind stress the ocean feels to be prescribed as climatology. This method of prescribing the wind stress does not alter the atmosphere and ocean model physics or

buoyancy fluxes. By removing the atmosphere's ability to respond to the anomalous SST in the ocean, in the form of atmospheric wind stress anomaly (e.g., weakened trades associated with an initial warm SST anomaly in the east), the Bjerknes feedback is deactivated, and ENSO events cannot develop. In this study, wind stress climatology is only prescribed along the equatorial Pacific basin (10°N-10°S, 120°E-60°W). Outside of this region, the CTRL and NoENSO experiments behave similarly with fully interactive atmosphere and ocean dynamics.

Throughout the NoENSO experiment, the atmospheric wind stress is communicated to the ocean component via the flux coupler. In the CTRL experiment, the total wind stress forcing the ocean can be represented by the following equation,

$$\tau_{total} = \tau'_{CTRL}(x, y, t) + \bar{\tau}_{CTRL}(x, y, t), \quad (3)$$

where  $\tau$  is the total wind stress felt by the ocean,  $\tau'_{CTRL}$  is the anomalous wind stress freely generated by the atmosphere model, and  $\bar{\tau}_{CTRL}$  is the seasonally varying climatological wind stress.

In the tropical Pacific in the NoENSO experiment, the ocean model overrides the total zonal and meridional wind stress with prescribed zonal and meridional wind stress from the seasonally varying monthly-mean climatology. The climatological values are calculated from the CTRL experiment and then interpolated to daily timescales. An application of a wind stress mask, shown in Figure 3.11 is the difference between experiments. The total wind stress the ocean feels in the NoENSO experiment is calculated using equation (4),

$$\tau_{total} = \alpha(\tau'_{CTRL}(x, y, t)) + \bar{\tau}_{CTRL}(x, y, t), \quad (4)$$

where  $\alpha$  defines the percentage of the anomalous wind stress generated by the atmosphere that passed to the ocean. As shown in Figure 3.11, between 5°N-5°S, the anomalous wind stress freely generated by the atmosphere has been set to zero and the ocean is only driven by the

CTRL's climatological wind stress. The magnitude of anomalous wind stress felt by the ocean is dependent on latitude within the tropical Pacific basin. Between 5°N -7°N and 5°S-7°S, the ocean feels the climatological wind stress along with 25% of the anomalous wind stress from the atmosphere. The amount of anomalous wind stress increases to 50% between 7°N -9°N and 7°S - 9°S and 75% from 9°N -11°N and 9°S -11°S to result in 100% of anomalous wind stress, generated by the atmosphere, forcing the ocean model at all latitudes higher than 11°N and 11°S. At these higher latitudes the NoENSO experiment operates similarly to the CTRL experiment (Larson et al., 2017). The gradual introduction of anomalous wind stress is used in the NoENSO experiment to avoid erroneous wind stress curl. This procedure will eliminate ENSO variability (see section 4.1) but allow the extra-tropics and other basins to operate similarly to the CTRL.

### **3.2.2 NoENSO Mean-state Comparison to CTRL**

Comparing the mean state of the CTRL and NoENSO experiments is an essential part of this study. We expect that asymmetry in ENSO amplitude project onto the mean state in the CTRL (Frauen et al., 2014). More specifically, El Niño events are stronger than La Niña events and bias the mean state slightly towards an El Niño state. As a result of ENSO variability being removed in the NoENSO experiment, the comparison of the two experiments should reflect a mean state bias from the CTRL that looks like a weak El Niño.

To accurately interpret the mean state comparison, it must be ensured that ENSO variability has been removed in the NoENSO experiment. This is done by calculating the Nino3.4 time series for both the CTRL and NoENSO experiment. The Nino3.4 time series for DJF, shows large anomalies in the CTRL and limited variability in the NoENSO experiment (Figure 3.12). However, weak anomalies are present in the NoENSO time series due to other

natural variability, such as tropical instability waves (Tian et al., 2019) and subtropical thermally coupled modes (Larson et al., 2018), that also drive SST variability in this region. The Nino3.4 annual cycle is used to ensure the temporal variability of the annual cycle is not affected when the wind stress is prescribed with the monthly mean climatological wind stress. Figure 3.13 shows that the annual cycle in the NoENSO experiment is similar to the CTRL with an average difference (NoENSO - CTRL) of  $0.04^{\circ}\text{C}$  and an average difference of  $0.01^{\circ}\text{C}$  in DJF, specifically. Slightly larger differences are present in the boreal summer and fall.

Figure 3.14 shows the DJF seasonal SST mean-state of the CTRL and NoENSO experiment. A similar climatological SST spatial pattern in both experiments indicates that altering the experimental design does not strongly affect the climatological SSTs in the NoENSO experiment. Figure 3.15 shows the spatial pattern of the difference between the two experiments (NoENSO - CTRL) over the tropical Pacific from ( $30^{\circ}\text{N}$ - $30^{\circ}\text{S}$ ,  $120^{\circ}\text{E}$ - $60^{\circ}\text{W}$ ). NoENSO is warmer than the CTRL by  $0.5^{\circ}\text{C}$  in the western equatorial Pacific and cooler than the CTRL by  $0.5^{\circ}\text{C}$  in the eastern equatorial Pacific. Figure 3.15 shows a La Niña like pattern; this is likely due to the CTRL climatology being biased towards El Niño (Frauen et al., 2014). A resulting weak El Niño signal is evident in the difference plots when comparing the experiments of the other variables used in this study.

Zonal SST climatologies were calculated by taking the average SST from  $5^{\circ}\text{N}$  - $5^{\circ}\text{S}$  at each longitude across the equatorial Pacific from  $120^{\circ}\text{E}$ - $60^{\circ}\text{W}$ . The zonal SST climatologies are shown in Figure 3.16 for all seasons in both experiments. The overall difference (NoENSO - CTRL) in the zonal DJF SST climatology is  $-0.01^{\circ}\text{C}$ , which is calculated by taking the average difference over all longitudes shown. The NoENSO experiment shows a slightly stronger zonal SST gradient during DJF, which is consistent with the CTRL's El Niño-like mean state bias

(e.g., weaker zonal SST gradient). Although not shown, small differences in the DJF SST climatologies are present in the northern Pacific, however the amplitude of the differences is generally small and reflects the El Niño-like mean state bias of the CTRL as mentioned above.

### 3.2.3 ENSO Variability Comparison to CTRL

Given that the CTRL climatology is biased towards El Niño, monthly anomalies for both experiments are calculated hereafter using the NoENSO reference climatology, shown in Equation (5) and (6). The anomalies are calculated as follows,

$$a'(x, y, t)_{CTRL} = a(x, y, t)_{CTRL} - \bar{a}(x, y, t)_{NoENSO}, \quad (5)$$

$$a'(x, y, t)_{NoENSO} = a(x, y, t)_{NoENSO} - \bar{a}(x, y, t)_{NoENSO}, \quad (6)$$

where  $a$  is a given variable of interest,  $a'$  is the monthly anomaly of the variable, and  $\bar{a}(x, y, t)_{NoENSO}$  is the monthly climatology in the NoENSO experiment.

To help demonstrate how using a different reference climatology can produce slightly different results, a latitudinal profile of composite El Niño and La Niña Z500 anomalies from the CTRL is calculated using both the CTRL Figure 3.17(a) and NoENSO Figure 3.17(b) reference climatology. The longitude of 96°W is chosen because Z500 anomalies driven by ENSO are large in North America near that longitude (see Figure 3.9(b) and (d)). When the CTRL experiment is used as the reference climatology for the CTRL ENSO composites, the amplitude of the El Niño and La Niña forced anomalies are relatively symmetric and similar in magnitude, despite El Niño SST anomalies being stronger than La Niña anomalies. However, when the CTRL ENSO composites are calculated using the NoENSO reference climatology, El Niño-related anomalies are much larger than La Niña-related anomalies at higher latitudes, as expected given that El Niño amplitude is larger. This suggests that because El Niño anomalies project onto

the CTRL mean-state, anomalies calculated using the CTRL reference climatology that is biased slightly towards El Niño, by definition, will underestimate composite anomalies associated with El Niño events and overestimate anomalies associated with La Niña. The end result is the teleconnected patterns appear similar in amplitude. However, using the NoENSO reference climatology that is not biased towards a particular ENSO phase maintains the asymmetry of the anomalies in the composites and clearly shows that the La Niña forced Z500 teleconnection pattern is weaker than that associated with El Niño.

In summary, two CESM1-CAM4 experiments are introduced, a CTRL and NoENSO experiment. Through comparing the DJF climatology of the CTRL and NoENSO experiment, we find that removing the anomalous windstress in the tropical Pacific does not strongly impact the mean-state in the NoENSO experiment. However, when taking the difference between the CTRL and NoENSO experiment, a weak El Niño like bias is present. This finding agrees with previous found ENSO-related asymmetries.

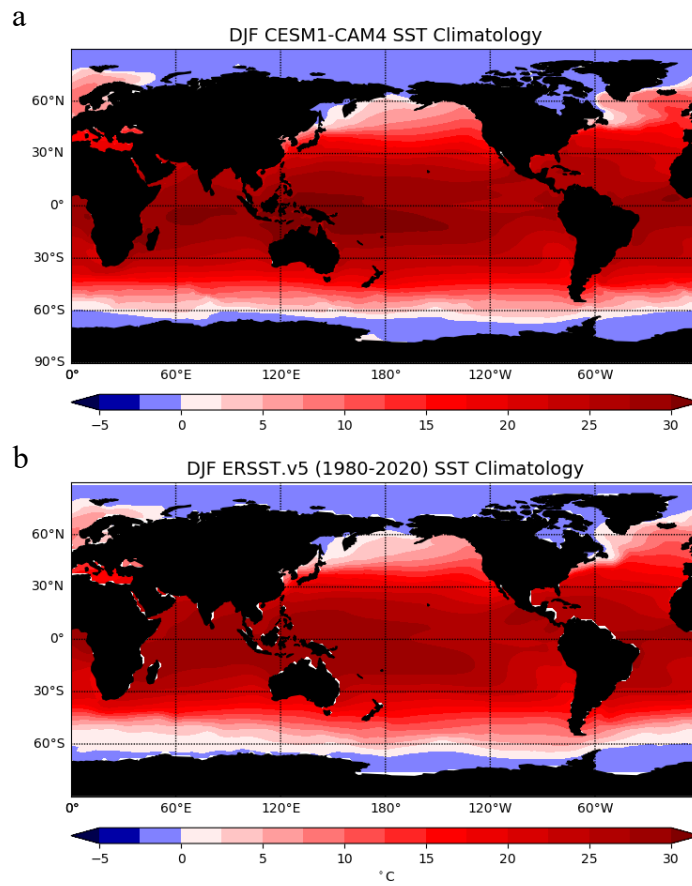


Figure 3.1: Seasonally averaged DJF SST Climatology. Units are °C. Top: CTRL experiment with 322 simulated years. Bottom: ERSST.v5 Reanalysis Data from 1980-2020. The ERSST.v5 has been detrended for accurate comparison with CTRL experiment.

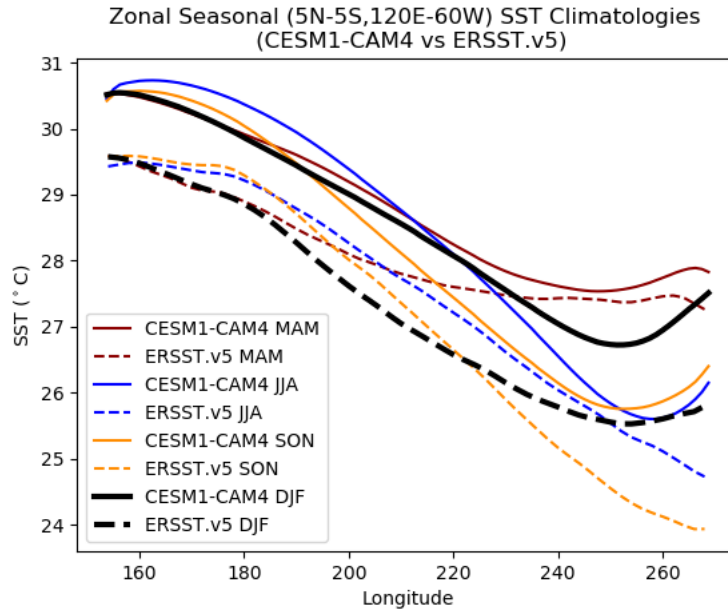


Figure 3.2: Zonal Seasonal SST Climatology across the equatorial Pacific Ocean (5°N-5°S, 120°E-60°W) in °C. Solid lines: Seasonal SST from the CESM1-CAM4. Dashed lines: Seasonal SST found in the ERSST.v5.

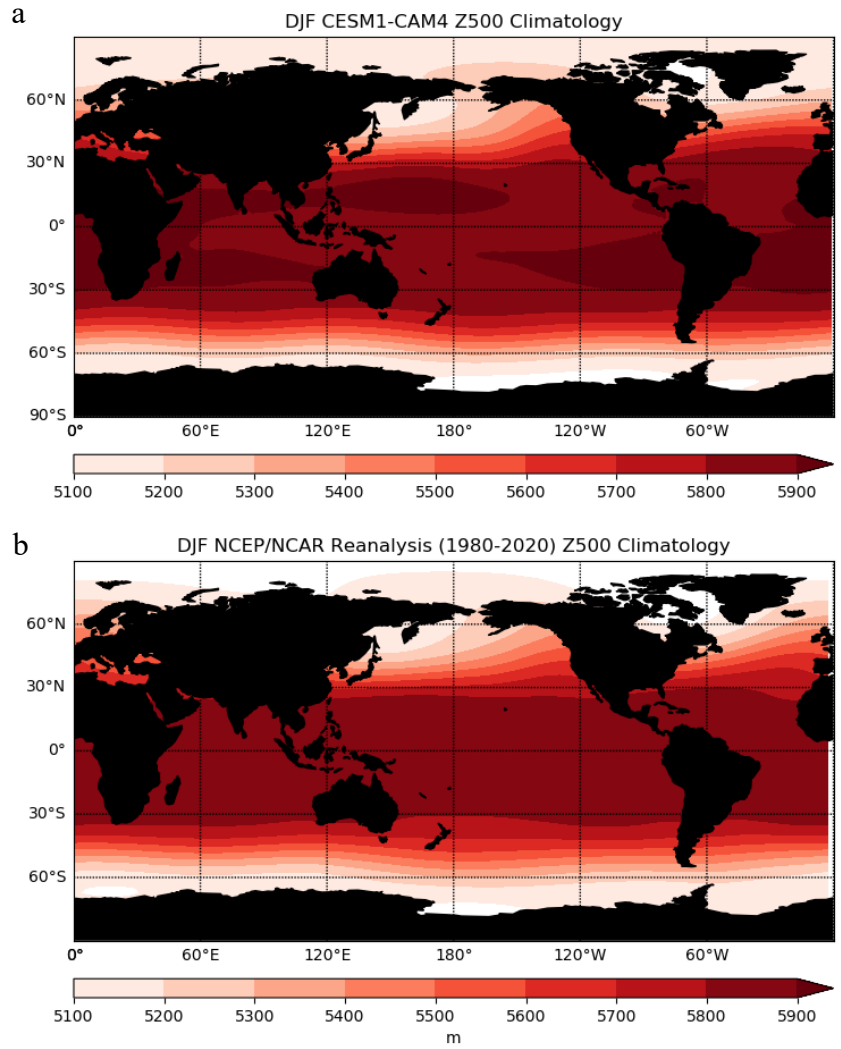


Figure 3.3: Seasonally averaged DJF Z500 Climatology. Units are in meters Top: CESM1-CAM4 CTRL experiment with 322 simulated years. Bottom: NCEP Reanalysis Data from 1980-2020. The NCEP dataset has been detrended for accurate comparison with CTRL experiment.

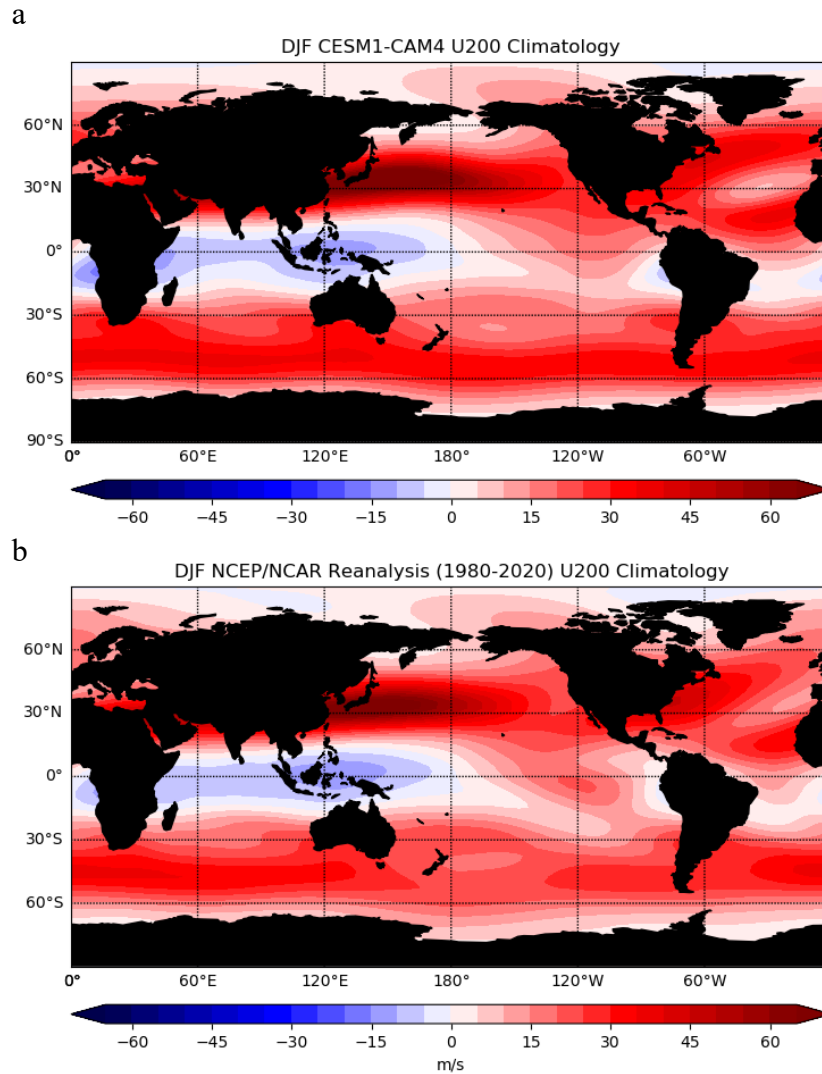


Figure 3.4: Seasonally averaged DJF U200 Climatology. Units are in m/s. Red shading is indicative of westerly winds speeds and blue shading represents easterly wind speeds. Top: CESM1-CAM4 CTRL experiment with 322 simulated years. Bottom: NCEP Reanalysis Data from 1980-2020. The NCEP dataset has been detrended for accurate comparison with CTRL experiment.

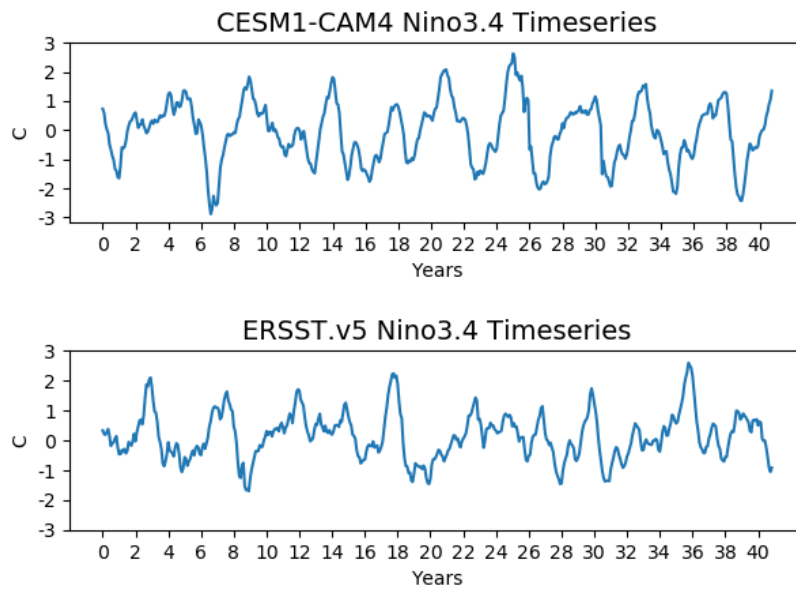


Figure 3.5: Area-averaged monthly SST anomalies over the Nino3.4 Region ( $5^{\circ}\text{N}$ - $5^{\circ}\text{S}$ ,  $120^{\circ}$ - $170^{\circ}\text{W}$ ). Units are in  $^{\circ}\text{C}$ . Blue line is the Nino3.4 Index calculated by the CESM1-CAM4 CTRL run. The orange line is the Nino3.4 time series from 1980-2020.

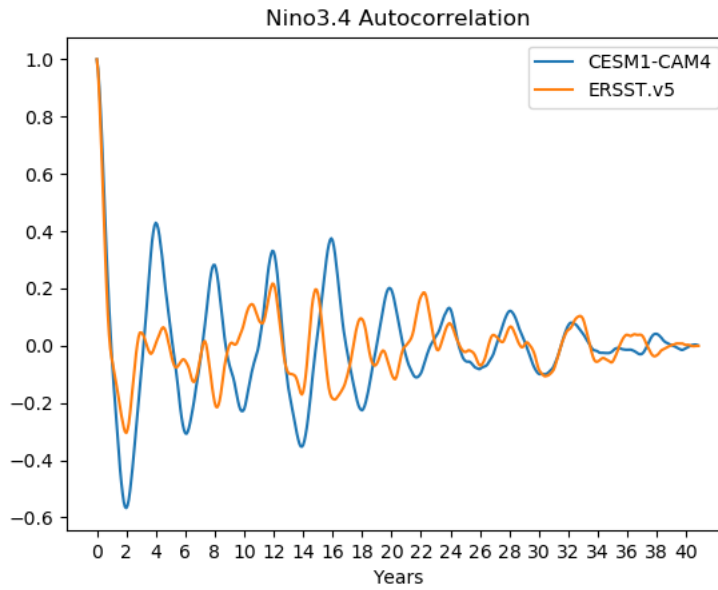


Figure 3.6: Autocorrelation of the Nino3.4 time series calculated using the area-averaged monthly seasonal SST anomalies over the Nino3.4 Region (5°N-5°S, 120°-170°W). Blue line is the autocorrelation of the CESM1-CAM4 CTRL experiment, only 40 simulated years are shown in this figure. The orange line is the Nino3.4 time series from 1980-2020.

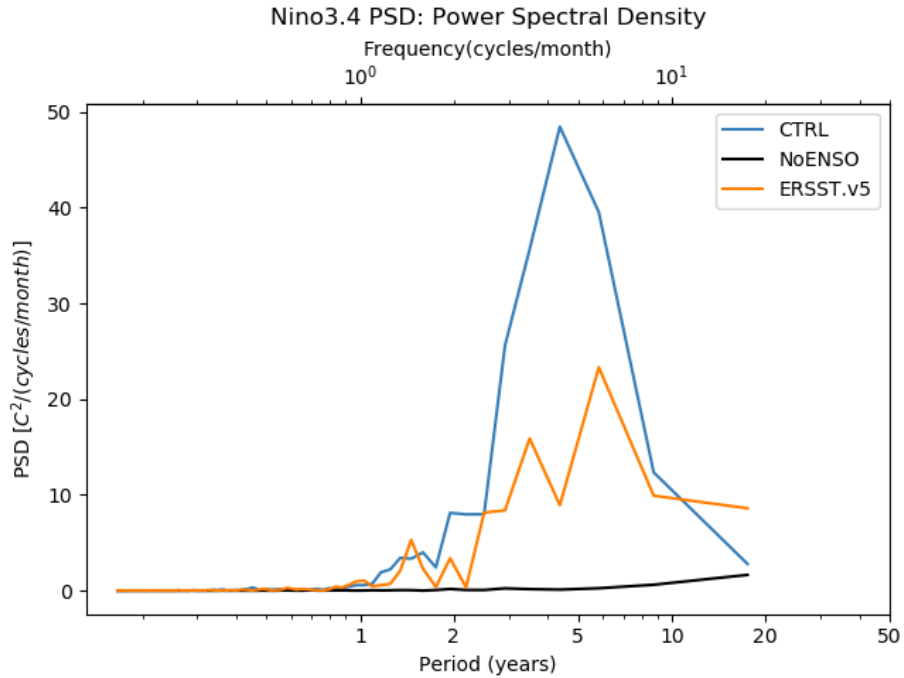


Figure 3.7: Power Spectrum with units  $^{\circ}C^2/(cycles\ month^{-1})$  of the Nino3.4 SST Index calculated using the area-averaged monthly SST anomalies over the Nino3.4 Region ( $5^{\circ}N-5^{\circ}S$ ,  $120^{\circ}-170^{\circ}W$ ). Blue line is the average spectra over 35-year segments from the CTRL experiment with 300 simulated years, The orange line is the detrended average spectra from 2 35-year segments from the ERSST.v5 1950-2020.

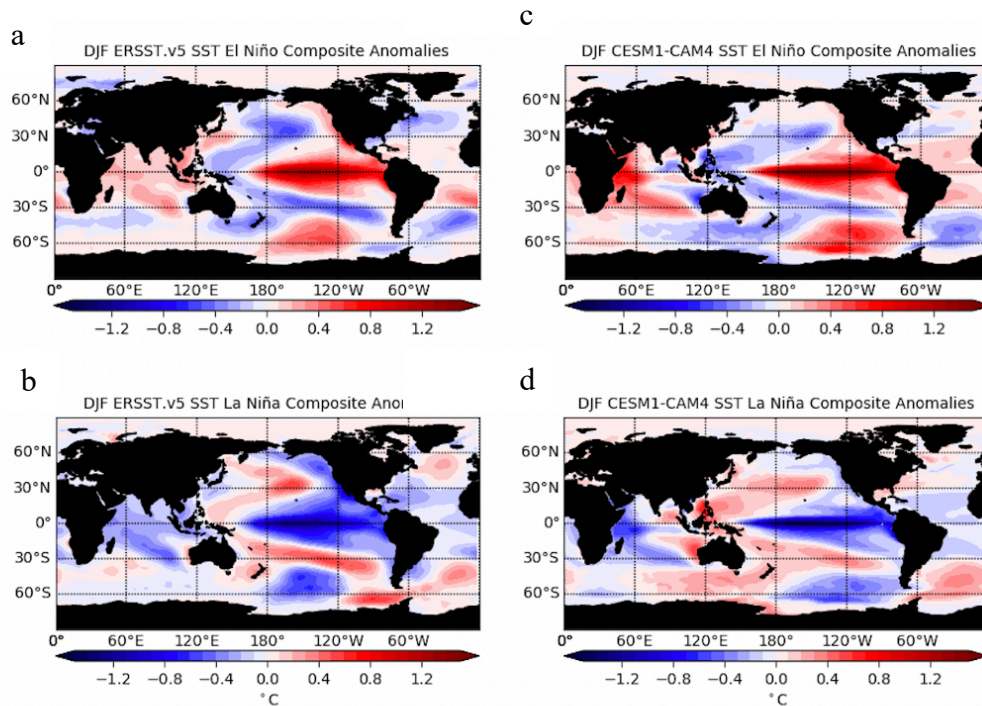


Figure 3.8: DJF SST ENSO composite anomalies are categorized based on a  $0.5^{\circ}\text{C}$  threshold. Anomalies are formed by removing the monthly mean SST from the CTRL experiment for a close comparison with observations. Units are in  $^{\circ}\text{C}$ . Red shading shows warmer than average surface temperatures and blue shading indicates cooler than average surface temperatures. El Niño composites are the top figures and La Niña composites are shown on the bottom. Left: Detrended ERSST.v5 data from 1950-2020. Right: CTRL experiment using 322 years of simulated data.

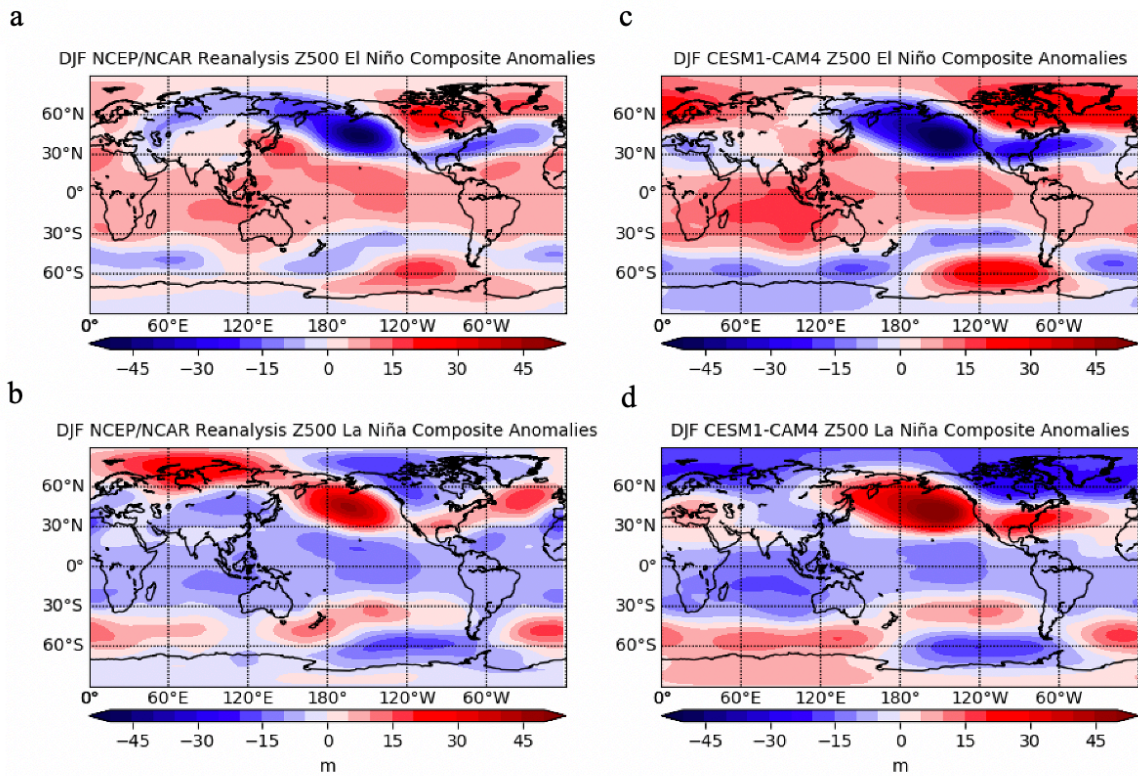


Figure 3.9: DJF Z500 ENSO composite anomalies are categorized based on a  $0.5^{\circ}\text{C}$  threshold. Anomalies are formed by removing the monthly mean Z500 from the CTRL experiment to closely compare with observations. Units are in meters. El Niño composites are the top figures and La Niña composites are shown on the bottom. Red shading shows higher than average heights and blue shading indicates lower than average heights. Left: Detrended NCEP Reanalysis data from 1950-2020. Right: CTRL experiment using 322 years of simulated data.

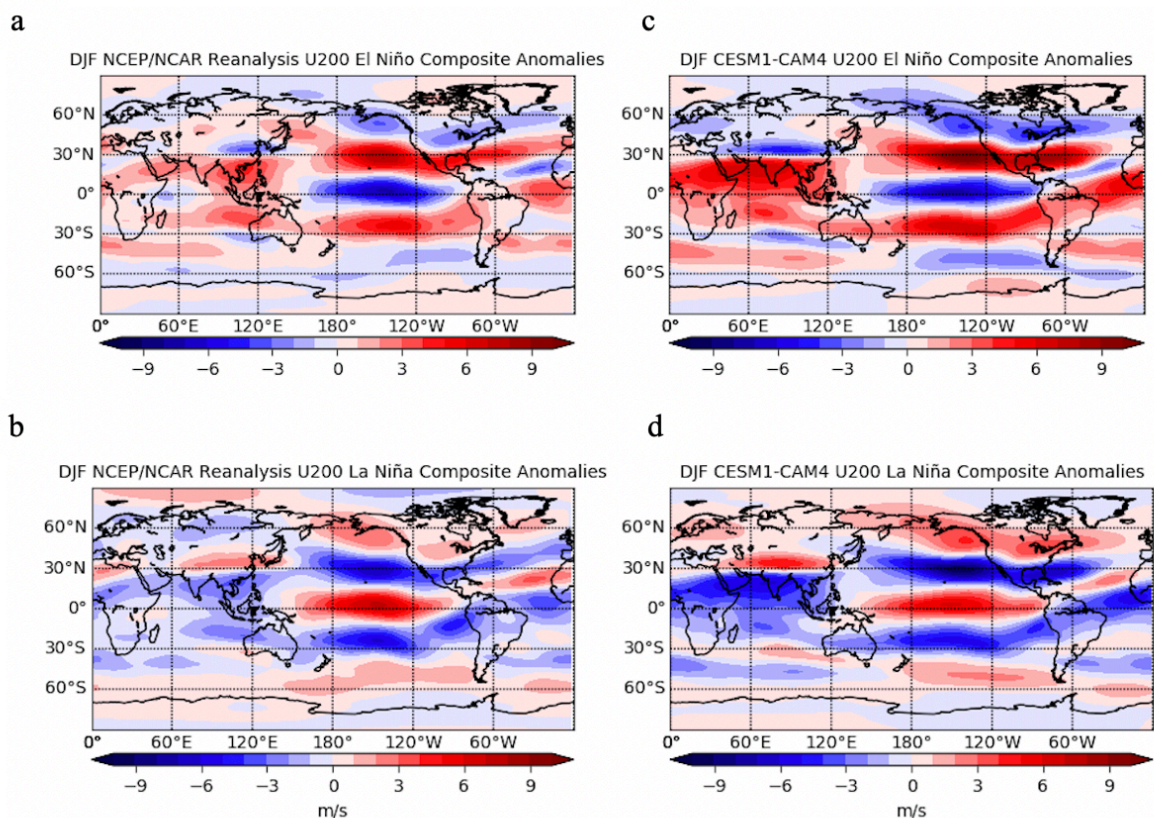


Figure 3.10: DJF U200 ENSO composite anomalies are categorized based on a  $0.5^{\circ}\text{C}$  threshold. Anomalies are formed by removing the monthly mean U200 from the CTRL experiment to closely compare with observations. Units are in m/s. El Niño composites are the top figures and La Niña composites are shown on the bottom. Red shading shows stronger than average winds speeds and blue shading indicates weaker than average wind speeds. Left: Detrended NCEP Reanalysis data from 1950-2020. Right: CTRL experiment using 322 years of simulated data.

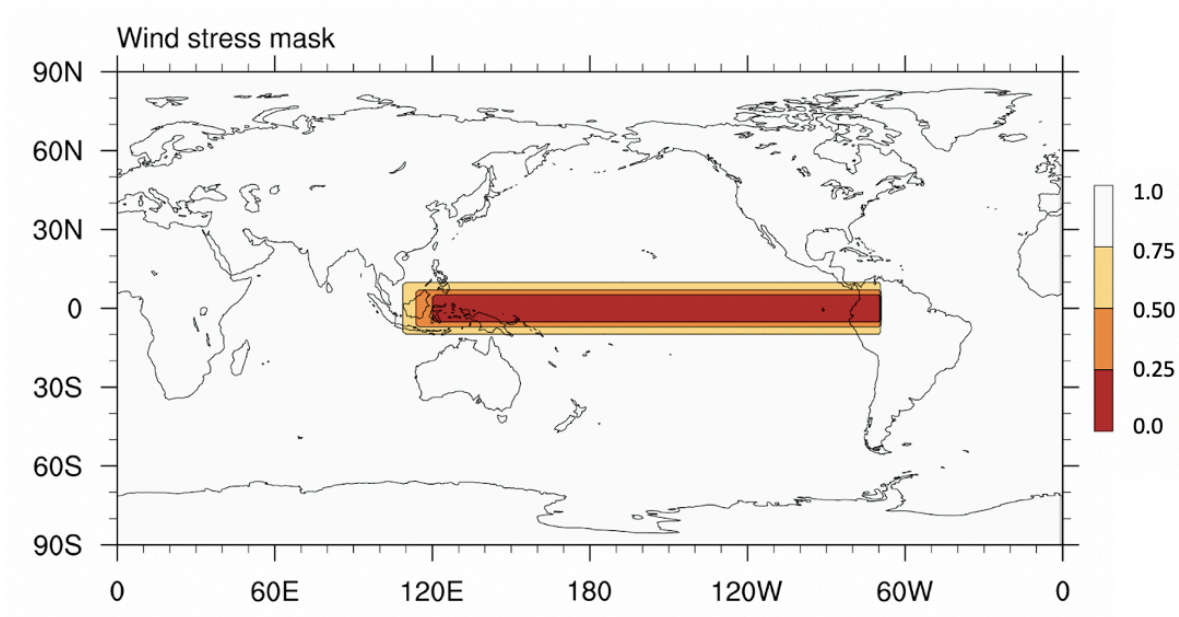


Figure 3.11: The global wind stress mask applied to the ocean component of the CESM1-CAM4. White: All the seasonally varying anomalous wind stress and the average monthly climatological wind stress can force the ocean component. Yellow: 75% of the seasonally varying anomalous wind stress and the average monthly climatological wind stress can force the ocean component. Orange: 50% of the seasonally varying anomalous wind stress and the average monthly climatological wind stress can force the ocean component. Red: 0% of the seasonally varying anomalous wind stress and the average monthly climatological wind stress can force the ocean component, only the seasonally varying climatology is felt by the ocean.

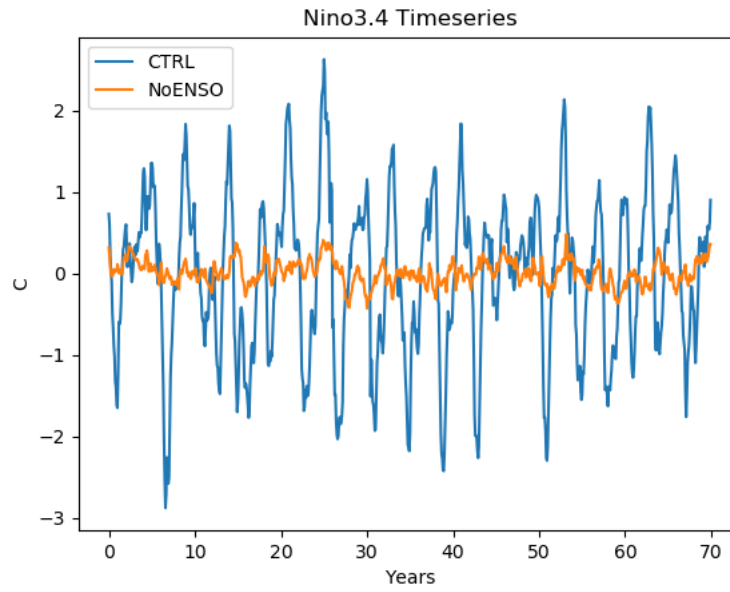


Figure 3.12: Area-averaged monthly SST anomalies over the Nino3.4 Region ( $5^{\circ}\text{N}$ - $5^{\circ}\text{S}$ ,  $120^{\circ}$ - $170^{\circ}\text{W}$ ). Units are in  $^{\circ}\text{C}$ . Blue line is the Nino3.4 Index calculated by the CTRL run. The orange line is the Nino3.4 time series from the NoENSO run.

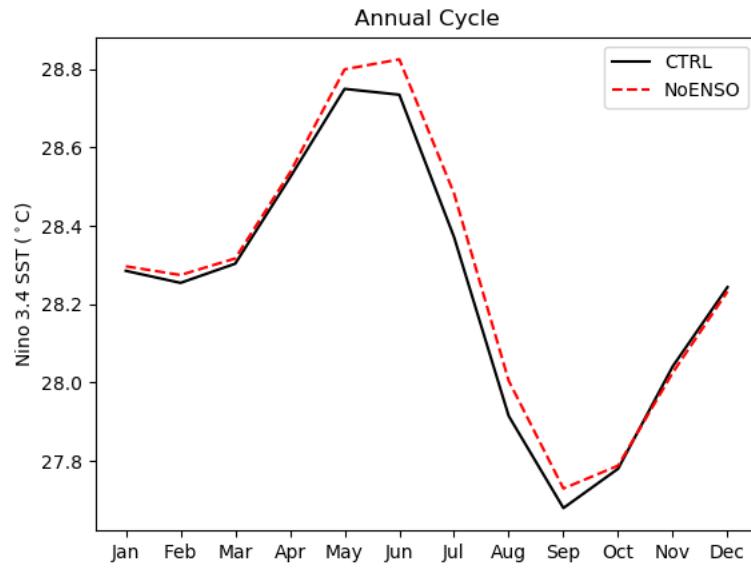


Figure 3.13: Annual cycle of SST averaged over the Nino3.4 region (5°N-5°S, 120°-170°W). Units are °C. Solid Black line is annual cycle from the CTRL. Dashed Red line is the annual cycle from the NoENSO.

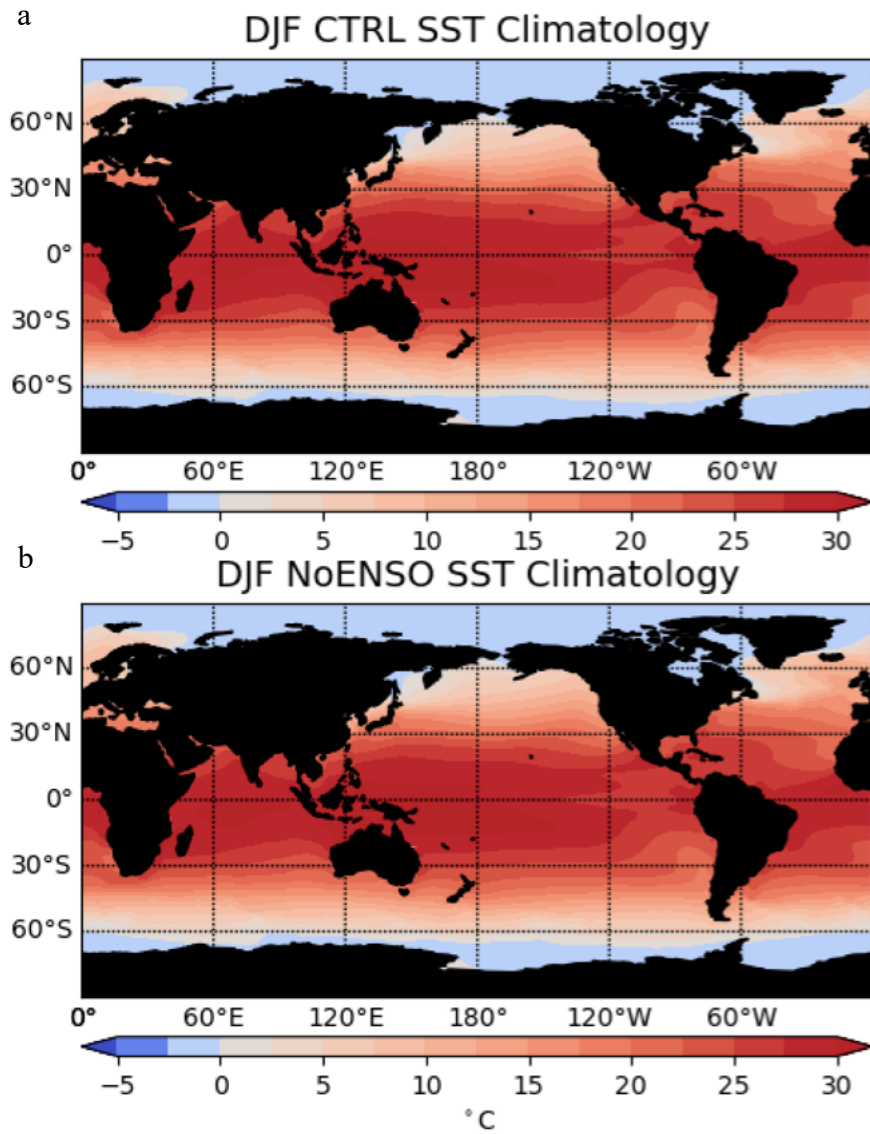


Figure 3.14: December-January-February (DJF) seasonal SST Climatology from the CESM1-CAM4. Units are °C. Top: CTRL experiment with 322 years Bottom: NoENSO experiment with 304 years.

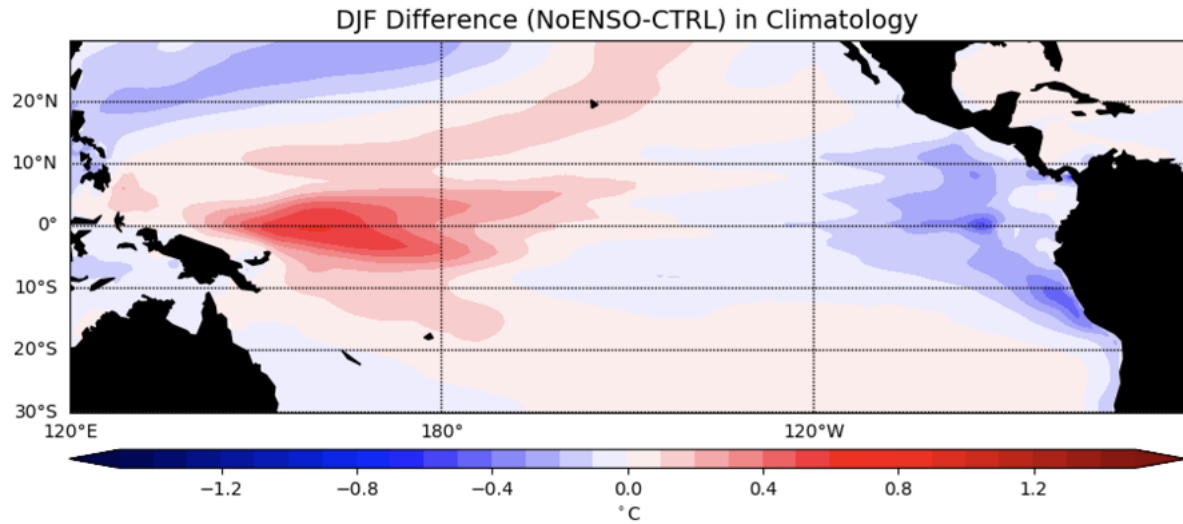


Figure 3.15: Difference (NoENSO-CTRL) between seasonal DJF SST Climatology across the equatorial Pacific basin (30°N-30°S,120°E-60°W). Units are °C. Red: Warmer SST in the NoENSO experiment. Blue: Cooler SST in the NoENSO experiment.

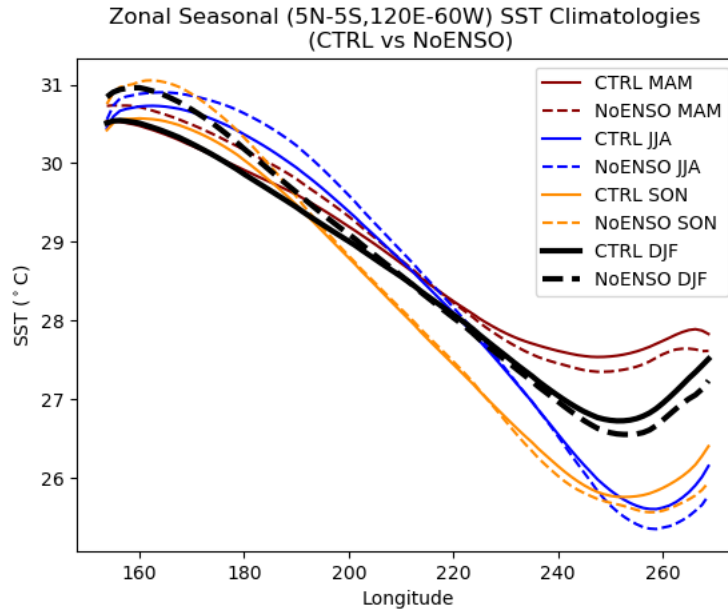


Figure 3.16: Zonal seasonal CTRL and NoENSO SST Climatologies across the equatorial Pacific (5°N-5°S, 120°E-60°W). Solid lines are seasonal averages from the CTRL. Dashed lines are seasonal averages from the NoENSO. Units are °C.

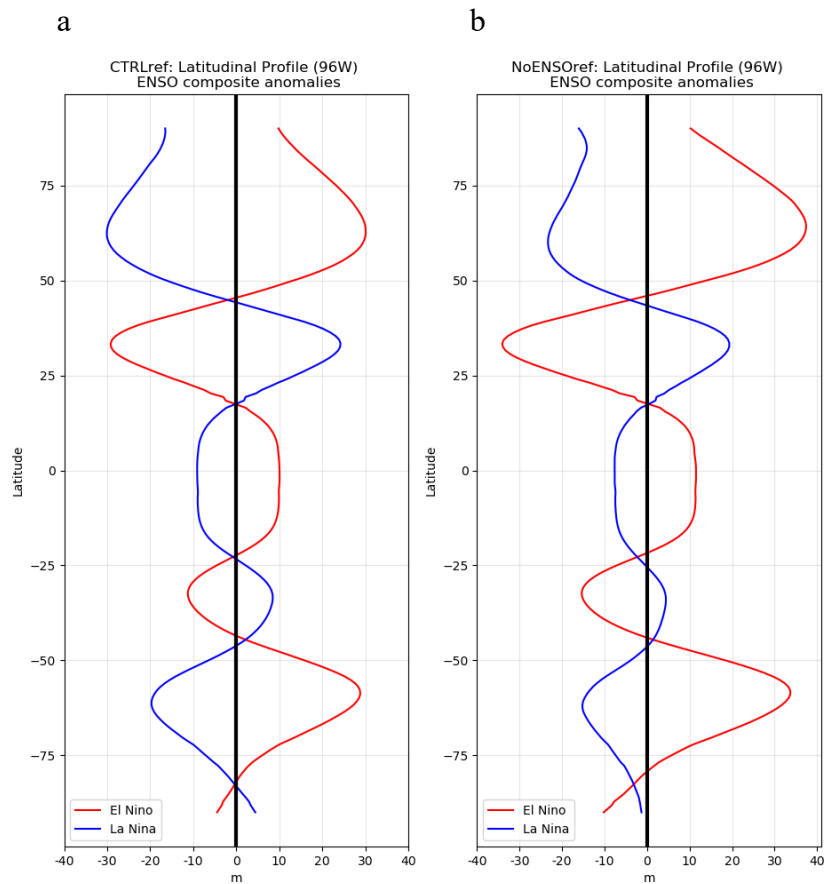


Figure 3.17: DJF Z500 El Niño and La Niña composite anomalies at the latitude 96°W. Units are meters. Red line is the El Niño composite anomaly. Blue line is the La Niña composite anomaly. Left: Composite anomalies calculated using the monthly mean from the CTRL. Right: Composite anomalies calculated using the monthly mean from the NoENSO.

## 4 Result: ENSO Impacts

The following section will address the following scientific question:

1. What are the atmospheric circulation and terrestrial impacts of ENSO over North America?

This question will be addressed by further analysis of the CTRL and NoENSO interannual variability.

### 4.1 Interannual SST Variability

First, interannual SST anomaly variance is calculated in the CTRL and NoENSO experiments to better understand the extent to which ENSO impacts interannual global SST variability. Figure 4.1 shows the interannual SST anomaly variance for the CTRL and NoENSO experiments. Based on visual inspection, the CTRL (Figure 4.1a) shows large variability in the equatorial ocean basins and along the western boundary currents. This agrees with typical features of interannual SST variability found during DJF (Busalacchi et al., 1983). In the NoENSO experiment, the SST variability in the equatorial ocean basins is substantially weaker as is the variability in the North Pacific, consistent with a lack of ENSO variability. To quantitatively compare the two experiments, the percent difference equation is used. The overall goal of using the percent difference equation, shown in section 2.3 (equation 1), is to quantitatively assess the ENSO-driven impacts on the ocean and atmosphere. Figure 4.2 shows the percent difference in SST variability between both experiments. It is evident that ENSO drives variability globally, specifically enhancing SST variability across all equatorial ocean basins and into the mid- and high-latitudes. For example, compared to the NoENSO experiment, ENSO variability in the CTRL increases SST variance in the tropical western Indian Ocean by

around 250% and by about 90% over a large region in the western tropical Atlantic. In the tropical Pacific, ENSO increases CTRL variability by about 800% in the western equatorial Pacific, 1000% in the eastern equatorial Pacific, and a maximum of about 4000% in the central equatorial Pacific. The large percent difference in the tropical basins are because variances in these regions are small in the NoENSO and CTRL experiments, causing differences between small numbers to play a major role in the resulting percentages. However, variance is large in the midlatitudes, and ENSO increases CTRL variability by 60% in the North Pacific. In Figure 4.2, ENSO reduces variability in several regions, as indicated by the blue shading. Specifically, ENSO reduces variability by an average of 20% in the western and central North Pacific, and by a maximum of 40% in a small region in the north central Atlantic.

## **4.2 Interannual Atmospheric Circulation Variability**

### **4.2.1 Interannual 500 hPa Geopotential Height Variability**

Geopotential height at 500 hPa is analyzed to aid in understanding ENSO's impact on atmospheric circulation variability. Similar to that done for SST, interannual variance plots are calculated for the CTRL and NoENSO experiments and shown in Figure 4.3. In the CTRL Figure 4.3(a), the regions with the largest variability in DJF are in the higher latitudes, particularly in the Northern Hemisphere with a large center of action near the Aleutian Low. A similar spatial pattern is shown in the NoENSO experiment (Figure 4.3(b)). The region of large variability in the North Pacific in the vicinity of the Aleutian low in the CTRL is also present in the NoENSO experiment, although differences in the magnitude of variance are present. The

magnitude and spatial pattern of large Z500 variability over North America is also different in the NoENSO experiment. To show this more quantitatively, a percent difference plot is used.

The percent difference plot for Z500 is shown in Figure 4.4. As expected, ENSO enhances variability in the tropics, as indicated by the monopole-like structure of increased variance. However, unexpectedly, ENSO reduces interannual variance in many regions around the world, specifically in the extra-tropics, shown by the regions of blue shading in Figure 4.4. In the extra-tropics, regions of reduced variability are often adjacent to the regions of enhanced variability, indicated by a dipole-like structure. This suggests that variability is displaced from one region, the region of reduced variance, into another region, the region of enhanced variance. This is particularly evident over North America, where a large region of enhanced variability is found over the southern U.S., which is located adjacent to the strongest region of reduced variability in the north central U.S., centered at (45°N, 96°W). Interannual atmospheric circulation variability over this region of North America is the focus of subsequent analyses in this work.

Next, the El Niño and La Niña composite anomalies for Z500, shown in Figure 3.9(b) and Figure 3.9(d), are calculated and used to aid in interpretation of the Z500 percent difference plot. As discussed previously, the large ENSO-driven Z500 anomalies are found in the higher latitudes, with a PNA-like forced atmospheric circulation pattern over North America. Strong anomalies during both ENSO phases occur off the west coast of North America and extend across the southeastern United States with strong opposite sign anomalies over Canada and most of the North Atlantic Ocean (Figure 3.9(b) and Figure 3.9(d)). These regions where ENSO drives strong Z500 anomalies correspond with the three main red shaded regions near North America in the percent difference plot (e.g., where ENSO enhances interannual Z500 variance). The region

of displaced variability in North America in Figure 4.4 is located where ENSO-driven anomalies are near zero in Figure 3.9(b) and Figure 3.9(d). To show this more clearly, we return to the latitudinal profile of Z500 ENSO composite anomalies along 96°W (Figure 3.17). The region of displaced variability is centered between 40°N-50°N. At these latitudes, the variance of Z500 anomalies for both El Niño and La Niña are close to zero whereas the adjacent latitudes show substantially enhanced variability. This suggests that ENSO preferentially drives variability to the north and southeast, away from the specified region, resulting in a PNA-like pattern. Further investigation is needed to determine if other tropospheric levels are impacted by the displacement of interannual atmospheric circulation variability.

#### **4.2.2 Interannual 200 hPa Zonal Wind Variability**

The position and strength of the North Pacific jet stream is an essential part in determining the seasonal climate over North America (Harrison and Larkin 1998; Ellis and Barton, 2013). For this reason, U200 is analyzed to investigate ENSO's impact on the jet. The CTRL interannual variance plot of U200, Figure 4.5(a), shows that large variability occurs in the tropical and midlatitude belts, particularly the regions over the Pacific Oceans. The strongest U200 variability occurs over the North Pacific Ocean and stretches across the southeastern United States. This is due to the various modes of climate variability that impact the Northern Hemisphere, which operate on time scales of a month and longer and prevent the zonal wind belts from becoming uniform and constant (Athanasiadis et al., 2010; Soulard et al., 2019). In NoENSO, Figure 4.5(b), U200 variance is reduced in both the tropical and midlatitude belts. The reduced variance in NoENSO is particularly evident in the Pacific along the Equator, and in the Southern Hemisphere. The U200 percent difference plot, Figure 4.6, confirms that ENSO

enhances variability in the equatorial, northern/southern midlatitude jet streams as well as the northern polar jet stream. ENSO enhances U200 variability over the north Indian and Atlantic Oceans, however, U200 variance in these regions is relatively low to begin with (e.g., Figure 4.5) and the large percent differences are likely due to total differences in variance that are relatively small compared to other regions of higher variability. Similar to Z500, latitudes of reduced variability are adjacent to latitudes of enhanced variability. This indicates that ENSO preferentially drives (e.g., displaces) variability to the north and south, reducing variability in latitudes that typically has variability during non-ENSO years. Next precipitation will be analyzed to investigate ENSO's impact on interannual variability at the surface.

### **4.3 Interannual Surface Variability**

#### **4.3.1 Interannual Precipitation Variability**

Given that ENSO preferentially drives middle and upper-level atmospheric variability into the northern and southern regions of North America, it is expected that ENSO drives North American precipitation variability as well. Interannual precipitation variance in the CTRL experiment shows large variability along the equatorial Pacific and Indian Oceans (not shown), consistent with ENSO variability. NoENSO interannual variance shows variability in similar regions as the CTRL, however, the variability is confined to the western Pacific warm pool region. The global percent difference in precipitation variance is shown in Figure 4.7. Due to noise in the data and to remove significant variance due to differences in small numbers, a significance level of 99% is used and an additional mask was applied to precipitation variability less than  $100 \text{ (mm month}^{-1})^2$  in the CTRL experiment. Based on Figure 4.7, ENSO enhances

variability across the Equatorial Pacific and Indian Oceans, as well as over certain regions in North and South Americas.

To further investigate precipitation variance over North America, the percent difference is calculated over  $12^{\circ}\text{N}$ - $70^{\circ}\text{N}$ ,  $160^{\circ}\text{W}$ -  $20^{\circ}\text{W}$ . Only the regions of significant variance difference are shown (Figure 4.8). ENSO enhances precipitation variability in two main regions over the United States, off the west coast and across the southeast. In the southeast, ENSO enhances variability by approximately 60%. As hypothesized, ENSO also displaces precipitation variability over the United States. The region of displaced variability stretches from  $30^{\circ}\text{N}$ , toward the central United States, to  $40^{\circ}\text{N}$ , in the eastern region of the United States. In this region, ENSO displaces approximately 20% of precipitation variability and is in a region where interannual variability is large in the United States, as shown in Figure 4.9.

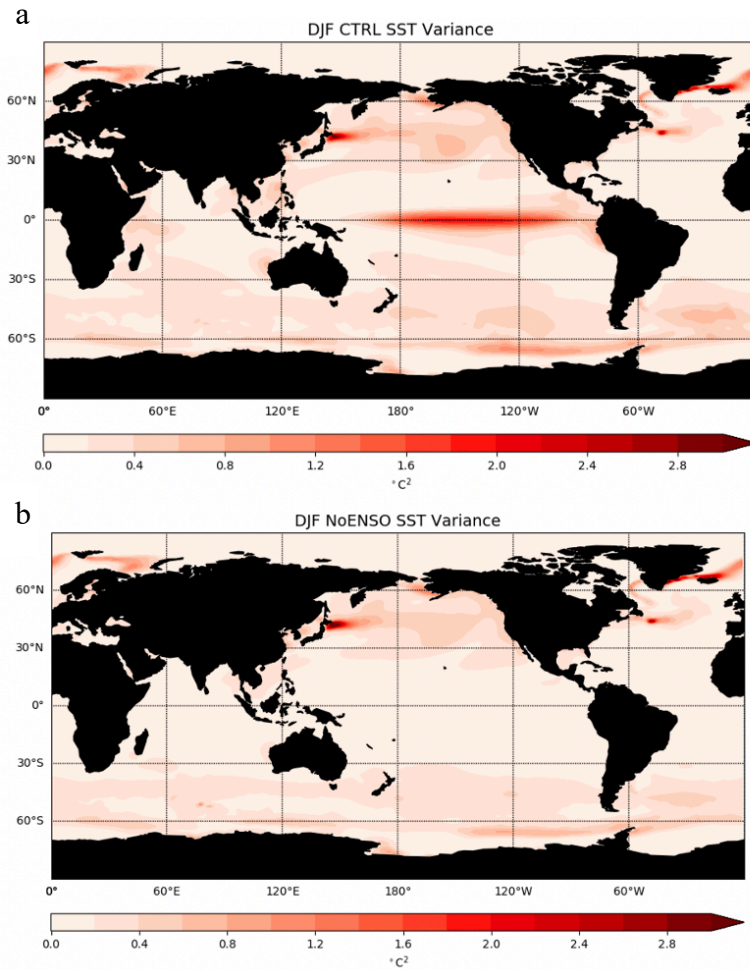


Figure 4.1: DJF Interannual sea surface temperature (SST) Variance. Top: Interannual variance from the CTRL run. Bottom: Interannual variance from the NoENSO run. Intervals of contours are 0.2 ( $^{\circ}\text{C}$ )<sup>2</sup>.

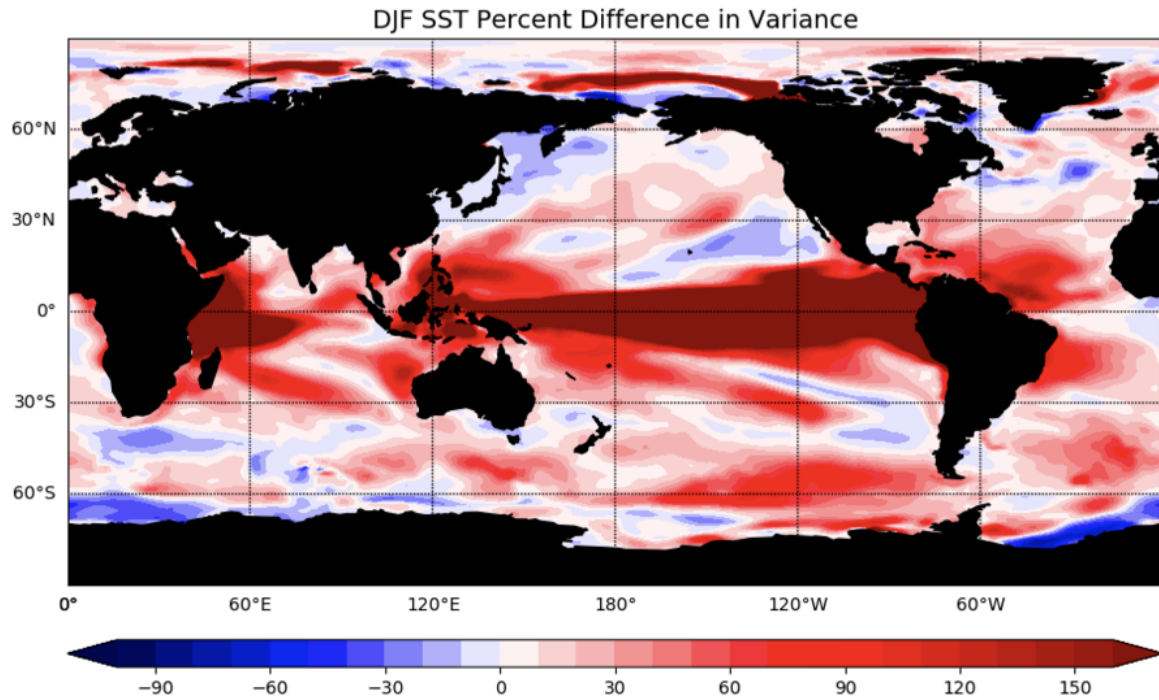


Figure 4.2 DJF SST Percent Difference of Interannual Variance. Red shading: ENSO increases variability. Blue shading: ENSO displaces variability. Grey shading: Insignificant values based on a 95% confidence level. Intervals of contours are 10%.

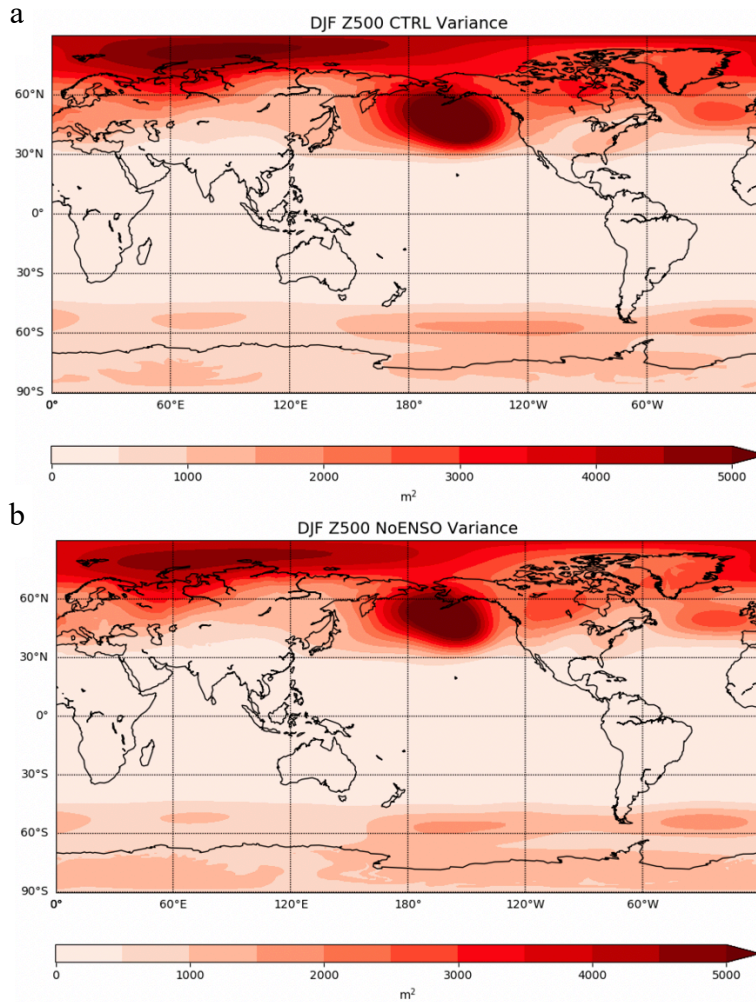


Figure 4.3 DJF Interannual 500 hPa geopotential height (Z500) Variance. Top: Interannual variance from the CTRL run. Bottom: Interannual variance from the NoENSO run. Intervals of contours are 500  $meters^2$ .

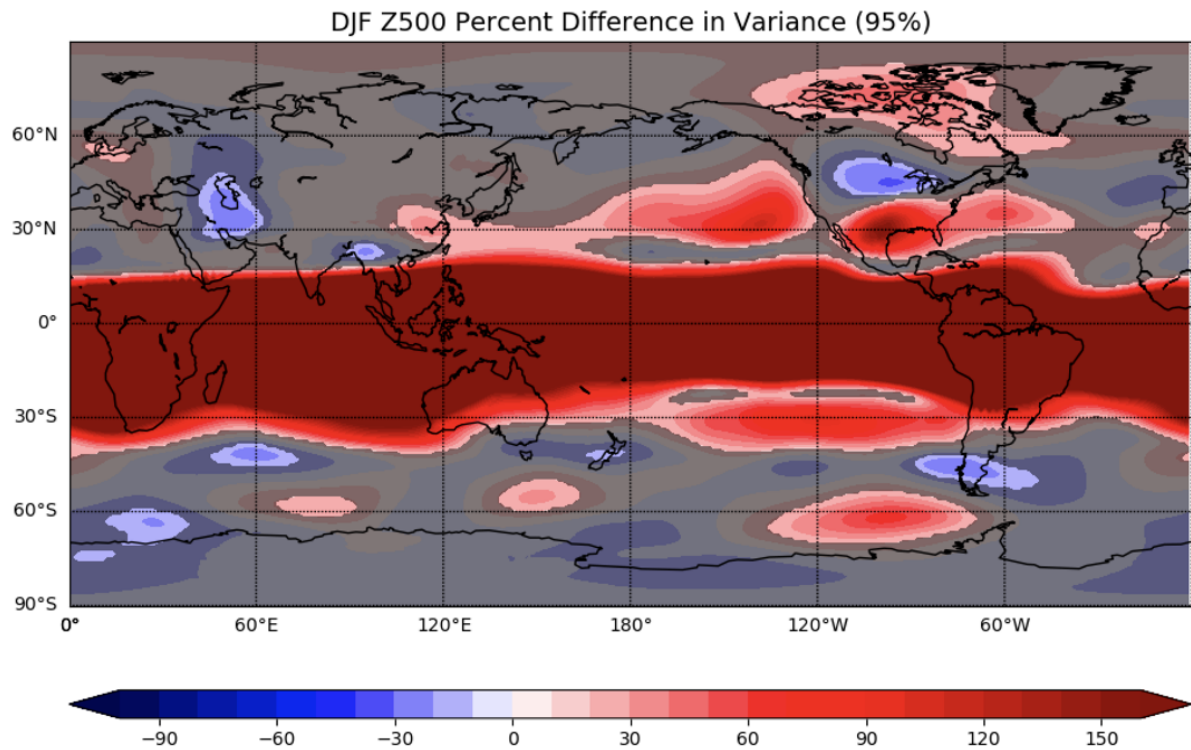


Figure 4.4 CESM1-CAM4 DJF Z500 Percent Difference of Interannual Variance, comparing ENSO and NoENSO. Red shading: ENSO increases variability. Blue shading: ENSO displaces variability. Intervals of contours are 10%. Grey shading: Insignificant values based on a 95% confidence level.

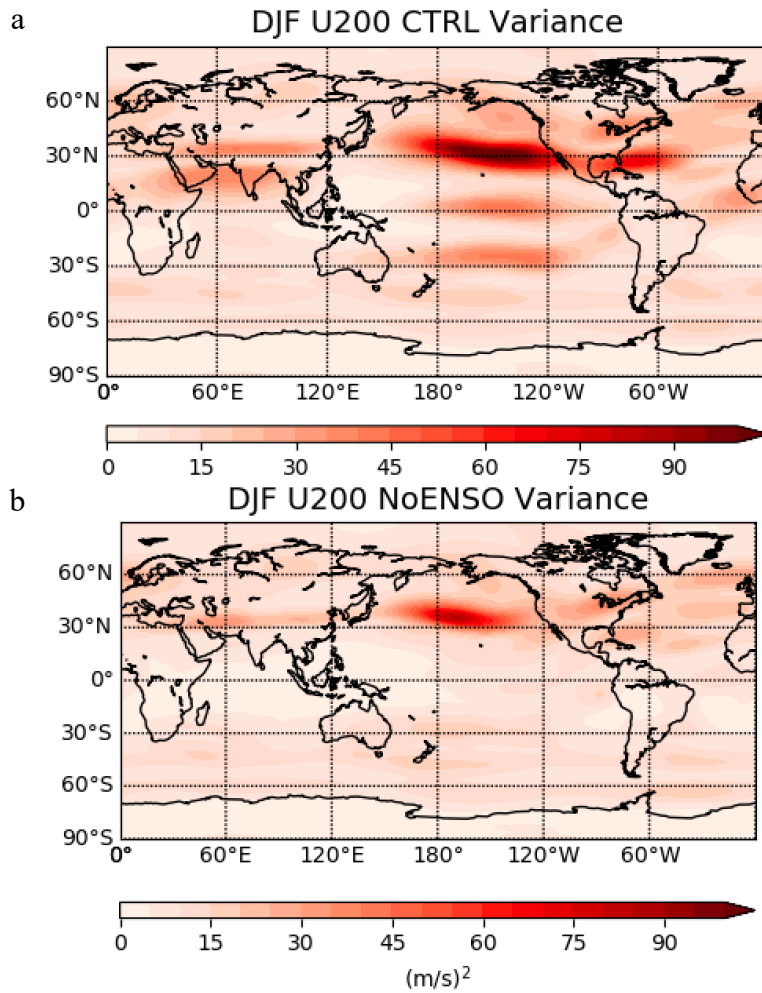


Figure 4.5 DJF Interannual 200 hPa zonal wind (U200) Variance. Top: Interannual variance from the CTRL run. Bottom: Interannual variance from the NoENSO run. Intervals of contours are  $5 (m/s)^2$ .

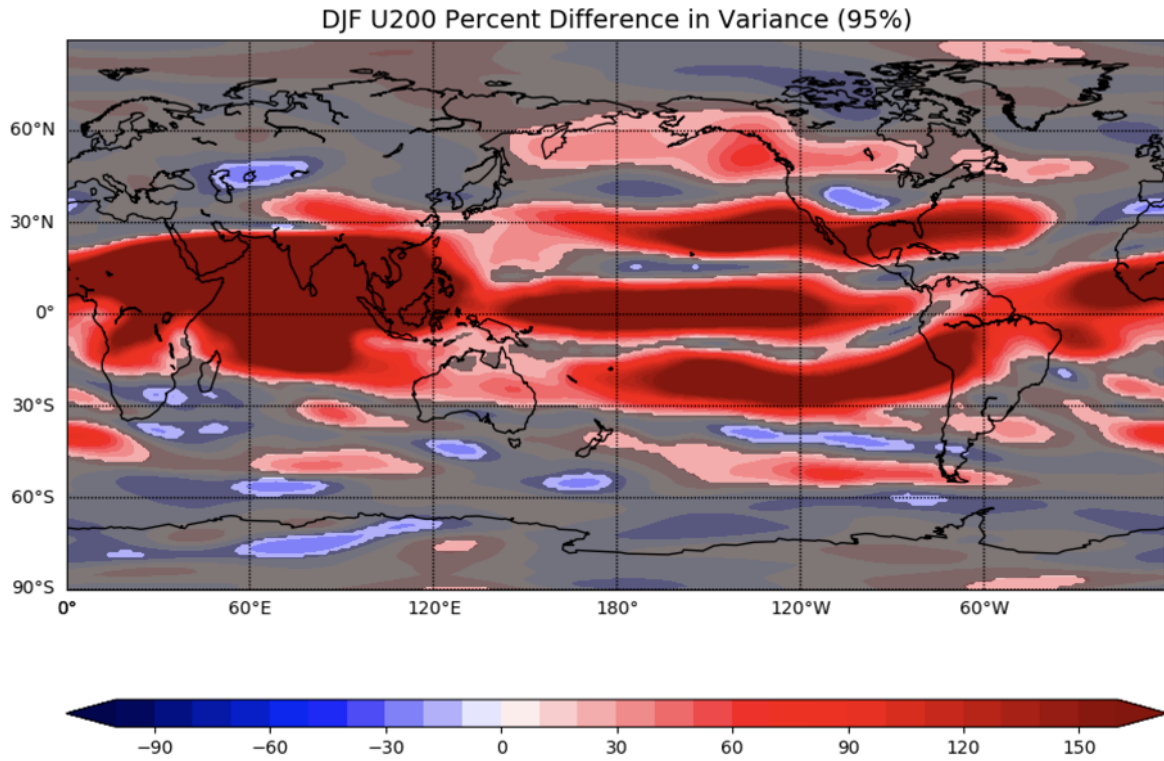


Figure 4.6: DJF U200 Percent Difference of Interannual Variance. Red shading: ENSO increases variability. Blue shading: ENSO displaces variability. Intervals of contours are 10%. Grey shading: Insignificant values based on a 95% confidence level.

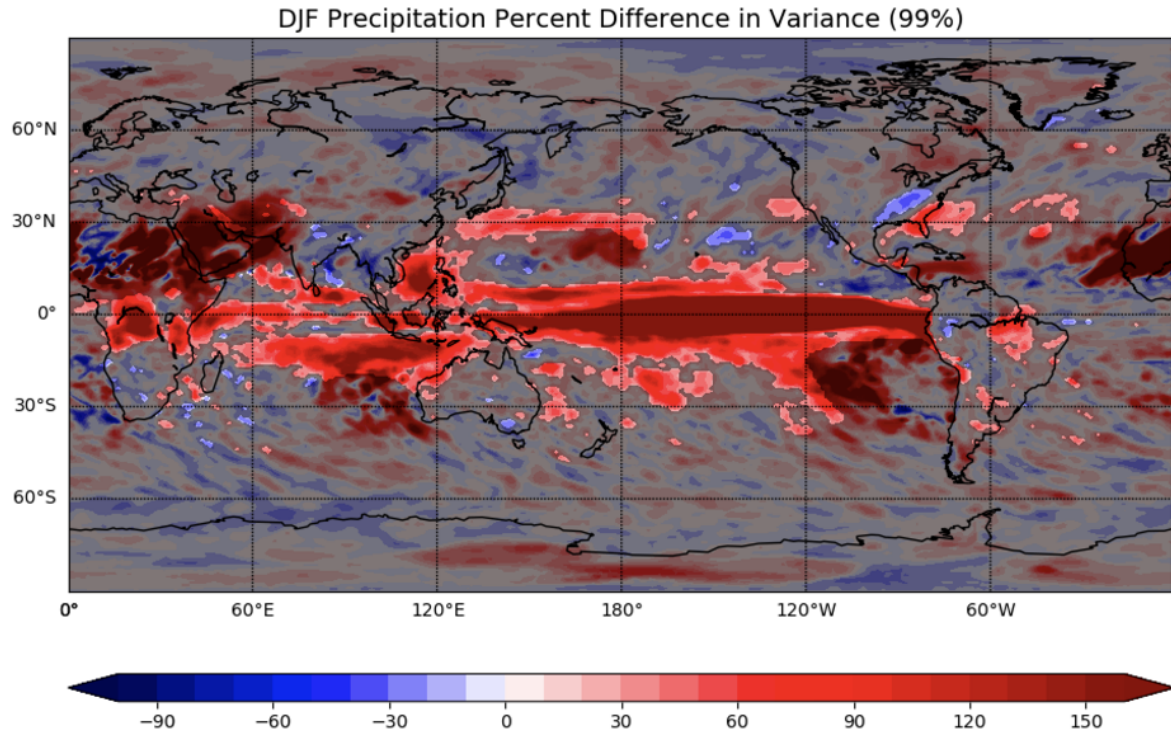


Figure 4.7 DJF Precipitation Percent Difference of Interannual Variance. Red shading: ENSO increases variability. Blue shading: ENSO displaces variability. Intervals of contours are 10%. Grey shading: Insignificant values based on a 99% confidence level, and  $100 \text{ (mm/month)}^2$  has been masked in the CTRL run.

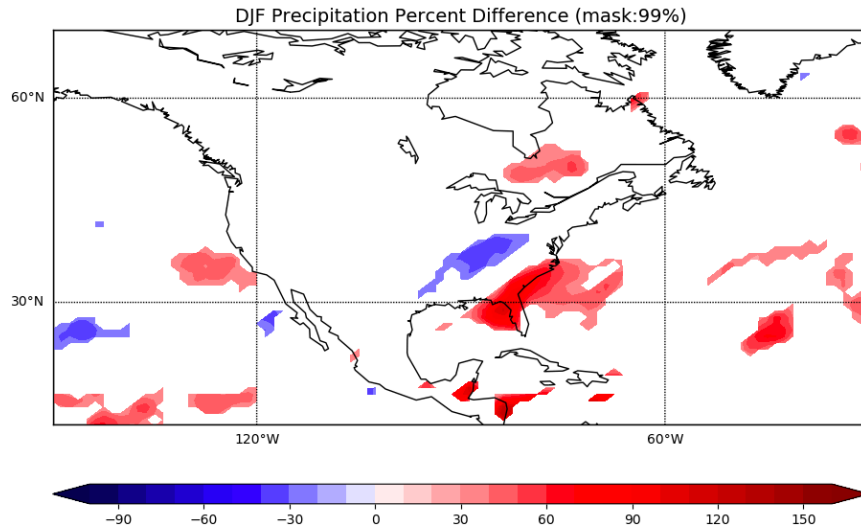


Figure 4.8 DJF Precipitation Percent Difference of Interannual Variance over North America. Red shading: ENSO increases variability. Blue shading: ENSO displaces variability. Intervals of contours are 10%. Insignificant values have been removed based on a 99% confidence level, and  $100 \text{ (mm/month)}^2$  has been masked in the CTRL run.

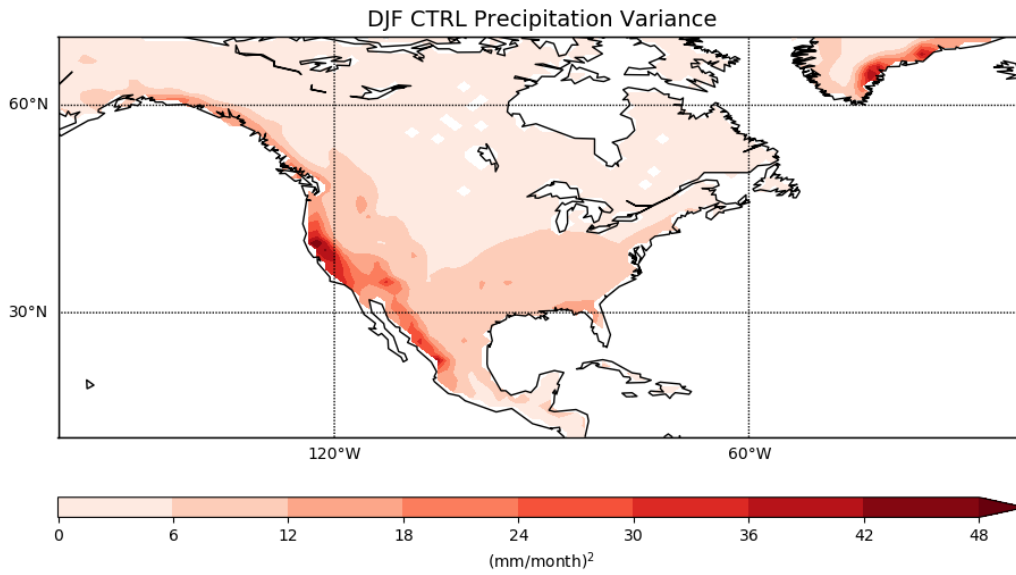


Figure 4.9: DJF Interannual Precipitation Variance. North American Interannual variance from the CTRL run. Intervals of contours are 200  $(mm/month)^2$ . Mask has been applied over the ocean. Precipitation Variance has been normalized based on CTRL climatological precipitation.

## 5 Result: Sensitivity to Sample Size

Large internal variability, unrelated to ENSO, in the atmospheric circulation can mask the ENSO signal and result in inaccurately determining the ENSO-forced response (Deser et al., 2018). For this reason, the focus of this section is to investigate the influence of sampling variability on determining the forced response to ENSO by addressing the following scientific questions.

1. Can the same ENSO-related patterns of enhanced and displaced variability over North America obtained from the model experiments also be derived from observations?
2. Are the results found in the CESM1-CAM4 model sensitive to the specified ENSO-neutral threshold?
3. How long of a record or simulation length is needed to resolve ENSO's impact on atmospheric variables over North America?

Each of these questions will be addressed in the following subsections.

### 5.1 Can the Model-Derived Signal be Obtained from Observations?

In previous sections, the percent difference in interannual anomaly variance is calculated using ENSO events in the CTRL and full NoENSO experiment from the CESM1-CAM4 model (Figure 4.4). However, it is not possible to fully remove ENSO from observational data (e.g., Compo and Sardeshmukh, 2010), so the closest comparison obtainable is the comparison between ENSO events and ENSO-neutral events in observations. ENSO-neutral years are used to represent the atmospheric circulation when variability due to ENSO is at a minimum and Niño3.4 SST variability is within a specified threshold. ENSO-neutral is defined as when the DJF Niño 3.4 SST anomaly is confined between a  $\pm 0.5^{\circ}\text{C}$  threshold. This is done to determine if

the displaced atmospheric circulation variability over North America found in Figure 4.4 is also extractable from observations. The percent difference equation (7) applied to observations is shown below,

$$\text{Percent Difference} = \left( \frac{\sigma_{ENSO}^2 - \sigma_{Neutral}^2}{\sigma_{Neutral}^2} \right) * 100, \quad (7)$$

where,  $\sigma_{ENSO}^2$  is the interannual variance of the combined El Niño and La Niña years, and  $\sigma_{Neutral}^2$  is the interannual variance of ENSO neutral years. Figure 5.1 shows the DJF Z500 percent difference plot computed using NCEP/NCAR reanalysis data and equation (7). Similar to what is found in the model experiment comparison results (Figure 4.4), ENSO enhances variability across the tropical Pacific and over much of North America. Three main regions of enhanced variability over North America are located off the west coast of the United States, across the southeastern United States, and in northern Canada. This pattern generally agrees with what is shown in Figure 4.4, however with differences in the spatial extent and amplitude in some regions.

A region of statistically significant displaced variability over the central-western United States is present in observations, although the location and amplitude of the displacement varies somewhat from what is found in the CESM1-CAM4 experiment comparison. A few possible reasons for this difference could be a difference in ENSO teleconnection patterns, the difference in threshold used to define ENSO neutral conditions, and the difference in sample sizes of ENSO and ENSO neutral cases. Based on previous studies showing that ENSO teleconnections in CESM1-CAM4 are generally realistic (e.g., Deser et al. 2012), we assume that model deficiencies in ENSO teleconnection patterns are not the primary contributor to the differences in the percent difference plots. The focus of the remainder of this study will be on the other two

potential factors, the difference in threshold used to define ENSO-neutral conditions, and the difference in the sample sizes of ENSO and ENSO-neutral events.

## 5.2 Sensitivity to the ENSO-neutral Threshold

The results found using the Z500 NCEP/NCAR reanalysis prompts the question, why is the spatial pattern in Figure 4.4 different from Figure 5.1? One possibility is that the threshold used for ENSO-neutral events in the reanalysis data ( $0.5^{\circ}\text{C}$ ) allows for larger Nino3.4 variability than occurs in the NoENSO experiment. In the NoENSO experiment, the Nino3.4 standard deviation is only  $0.17^{\circ}\text{C}$ . This could result in more tropical forcing of the extra-tropics allowed in the NCEP/NCAR reanalysis results compared to when using NoENSO as the ENSO-neutral dataset. A useful test is to see if a similar spatial pattern is shown in the CTRL CESM1-CAM4 experiment as found in observations based on the same  $0.5^{\circ}\text{C}$  threshold. Recall that the CTRL exhibits pronounced ENSO variability (Figure 3.12), so years can be separated into ENSO versus ENSO-neutral, similar to that done in observations. If the CTRL results match the observations, then the issue is that the threshold for ENSO-neutral is not strict enough in the observational analyses to fairly compare to the NoENSO experiment.

The same equation (7) was applied to DJF Z500 anomalies from the CTRL CESM1-CAM4 experiment. Figure 5.2 shows that the observational spatial pattern is not replicated in the CTRL when using the same  $0.5^{\circ}\text{C}$  threshold for ENSO neutral. The regions of enhanced variability over North America are similar to the regions seen in observations with enhanced variability off the west coast, the southeast United States, and parts of northeast Canada. However, the region of displaced variability seen in the central western region in observations is not present in the CTRL pattern. Therefore, matching the thresholds for ENSO-neutral for the

observations and CTRL calculations do not result in similar patterns, suggesting the ENSO threshold is not the main contributor to the pattern differences.

Not only does the spatial pattern look different when comparing the CTRL with observations, but the CTRL pattern also differs from the original calculation done using the NoENSO experiment to represent ENSO neutral variability (Figure 5.2). The only difference between the calculation in Figure 4.4 and the calculation in Figure 5.2, is the data used to estimate the ENSO neutral variance. In Figure 5.2, ENSO neutral is based on a  $0.5^{\circ}\text{C}$  Nino3.4 threshold, however in the experiment comparison, Figure 4.4, the average deviation of the Nino3.4 is only  $0.17^{\circ}\text{C}$ , therefore the typical ENSO neutral variability in NoENSO is well below the  $0.5^{\circ}\text{C}$  threshold. A major contributing factor could be this difference in amplitude of SST variation in the Nino3.4 region between the NoENSO experiment and the CTRL ENSO-neutral years. To test this, a more restrictive ENSO-neutral threshold is applied to the CTRL experiment. Here, an ENSO neutral event is defined as when the magnitude of SST variability in the CTRL Nino3.4 region is within the NoENSO average deviation ( $0.17^{\circ}\text{C}$ ). By reducing the ENSO-neutral threshold, the sample size changes from 200 ENSO events and 100 neutral events with the  $0.5^{\circ}\text{C}$  threshold, to 260 ENSO events and 40 neutral events with the  $0.17^{\circ}\text{C}$  threshold. Figure 5.3, shows that even when the ENSO threshold is restricted to  $0.17^{\circ}\text{C}$  in the CTRL, the location of the regions of enhanced variability is different from when NoENSO is used to estimate ENSO-neutral variability and the region of displacement does not emerge over North America. These findings suggest that the differences in the spatial patterns are likely not primarily due to differences in the threshold used to define ENSO-neutral.

### 5.3 Sensitivity to Sampling Variability

The final potential contributing factor to consider when explaining the difference in the North American spatial patterns, specifically the regions of displacement, is the sample size of ENSO-neutral events used in each computation. In the CESM1-CAM4 model experiment comparison (Figure 4.4), ENSO-related variance is calculated over 260 ENSO years from the CTRL experiment and the non-ENSO variance is calculated over the full 300-yr NoENSO experiment (i.e., 300 ENSO neutral years). When instead using the CTRL experiment to sample ENSO-neutral years, there are only 40 neutral years that are within the “very neutral” threshold of  $0.17^{\circ}\text{C}$  estimated by the NoENSO Nino3.4 standard deviation. The number of ENSO years and the ENSO-related variance is identical for both methods. This difference motivates the question, are the results sensitive to the sample size of ENSO-neutral years?

If 40 very ENSO-neutral years is not enough to resolve the displaced region over North America when using the CTRL ENSO-neutral years, then it is reasonable to hypothesize that only using 40 years from the NoENSO experiment to compute the non-ENSO variance also will not resolve the amplitude of the reduced variability in the region of displacement. Figure 5.4 shows the result of using equation (1), same as the original figure, Figure 4.4, but the number of NoENSO years is limited to the same number available in the CTRL experiment (40 years of DJF averages). When using this one random sample of 40 years from the NoENSO experiment, the displaced region does not emerge. The method is repeated using multiple 40-year random samples. The spatial pattern changes with each random sample, suggesting that the resulting spatial patterns are dependent on which random 40 NoENSO years are used. For this reason, this method is repeated using various sample sizes to identify when sensitivity in sample size begins to diminish.

The Monte Carlo random sampling method is a pseudo-random number generator that is commonly used to repeatedly generate random samples for statistical analyses. The overarching goal of using this method is to test sample size sensitivity, through the visualization of variability of same-size random NoENSO samples. Our initial estimate to resolve the displacement is 300 NoENSO years, since this is the total length of the NoENSO experiment and a significant displacement exists when using all 300 years. The initial step of this method is to select the sample sizes that will be tested here sample sizes of 20, 40, 60, 80, ..., 300 years are selected. Next, the Monte Carlo simulation randomly selects N years (or DJFs) with replacement, where N is the sample size, from the 300-yr long NoENSO simulation. This step is repeated 10,000 times to generate 10,000 samples for each sample size. Next, the ENSO-neutral interannual variance is calculated for each sample at each sample size. Two regions over North America are specified, one region where ENSO reduces Z500 variability (43°N-47°N, 105°W-95°W) and one region where ENSO enhances Z500 variability (27°N-33°N, 105°W-95°W). The area-weighted average NoENSO variance is calculated at both locations for all samples at each sample size. Finally, the ensemble average NoENSO interannual variance is calculated by averaging the area-weighted average interannual variance over all iterations at each sample size. This value is used to calculate the percent difference using the original equation (1). The ENSO variance is constant across all sample sizes and is estimated from the 260 ENSO events specified in previous sections.

Figure 5.5 shows the results of the Monte Carlo simulation over the region where Z500 variance is reduced over North America. The blue dots represent the percent change based on the average NoENSO variance at each sample size. The error bars signify the percentage of uncertainty of the percent change, which stems from variability between independent NoENSO

random samples. We define the “truth” as the percent change estimated from the full 300-yr sample size of ENSO-neutral years. The uncertainty decreases with increasing sample size, as expected. When the full 300-yr NoENSO time series is used to estimate the ENSO-neutral variance, the results show that ENSO drives a 25% reduction in Z500 variance over the Northern United States and Southern Canada. The result is underestimated by about 4% at the smallest sample size of 20, with ENSO driving a 21% reduction in Z500 variance. The large uncertainty at smaller sample sizes suggests that a wide range of results are possible. For example, when a subset of 20 random very neutral years is used, the resulting percent change can range from an increase in variance of 80% to a reduction in variance of about 125%. The upper and lower bounds of the percentage of uncertainty with a sample size of 20 are drastically different than what is defined as the “truth” value of the percent change with a sample size of 300. The average magnitude of the displacement (-25%) appears to be resolved when roughly 60-80 ENSO neutral years are used in the calculation, although the uncertainty is too large to confidently expect consistent results across different samples. It is not until the sample size increases to 240 years that the uncertainty drops to within 10% of our “truth” estimate.

The results of the Monte Carlo simulation over the Z500 enhanced region are shown in Figure 5.6. Similar to Figure 5.5, the dots represent the percent change based on average NoENSO variance at each sample size, and the error bars are the percentage of uncertainty between independent NoENSO random samples. When the full sample size of 300 years is used to estimate ENSO-neutral variance, the results show that ENSO increases variance in this region by roughly 155%. Opposite of what occurs in the displaced region, in the enhanced region the percent change is overestimated at the sample size of 20 years by about 10%, with ENSO estimated to increase the variance by 165%. The average magnitude of the enhanced variance

appears to be resolved when roughly 100 ENSO neutral years are used, although the uncertainty is large. It is not until the sample size increases to 180 years that the uncertainty drops to within 10% of our “truth” estimate.

Similar to Z500, the Monte Carlo approach is also applied to the regions of reduced (35°N-41°N, 90°W-80°W) and enhanced (30°N-34°N, 81°W-74°W) interannual precipitation variability in Figure 4.8. When all 300 years are used, ENSO is found to reduce precipitation variance by 25% in the displaced region. In the enhanced region, ENSO increases the variance by 58%. The percent change is underestimated in the reduced variance region and overestimated in the enhanced region at smaller sample sizes, similar to that seen for Z500. For the reduced variance region, a sample size of 240 very neutral years is required for the uncertainty to be within 10% of our “truth” estimate. For the enhanced region, 220 years are required.

Based on findings from both the Z500 and precipitation sample size sensitivity experiments, an estimated 240 of very neutral years are needed to diminish sensitivity to sample size. However, some impacts will be resolved in as little as 180 years. The sign of the impacts, whether variance will be enhanced or reduced, may be resolved at smaller sample sizes, but not consistently due to the large uncertainty. These results imply that a multi-century simulation length of approximately 1800 model years is needed to resolve the full impact of ENSO on interannual atmospheric variability, based on the ratio of 260 ENSO to 40 very ENSO neutral years obtained from the CESM1-CAM4 CTRL run.

#### **5.4 Testing the Sample Size Hypothesis**

The CESM2 is used to test the hypothesis that if a simulation is long enough to contain 240 very ENSO-neutral cases, sensitivity to sample size will diminish and the full impact of

ENSO on interannual atmospheric variability can be resolved. To investigate this hypothesis, the full 2000-yr CESM2 simulation is used. This simulation length surpasses the previously stated 1800 model years needed to obtain 240 very ENSO neutral years. ENSO is categorized based on the same definition used above, where an ENSO-neutral event is defined as when the magnitude of SST variability in the CTRL CESM2 Nino3.4 region is within the NoENSO average deviation ( $0.17^{\circ}\text{C}$ ). However, this results in only 195 very ENSO-neutral years and shows that the ratio of ENSO years to ENSO-neutral years can vary from model to model. Although this amount is slightly less than the number recommended, the sensitivity analysis suggests that the sign of the percent change should be reproduced with this slightly smaller ENSO neutral sample size. The CESM2 DJF Z500 ENSO and ENSO-neutral events are used in equation (7) to produce a percent difference plot, shown in Figure 5.7. A similar spatial pattern is shown in Figure 5.7 as what is seen in the original Figure 4.4, with enhanced variability off the west coast of the United States, near the Aleutian Low, and across the southern United States. A significant yet small region of reduced variability is present over the north central region of the United States into Canada, which is in the same general location as shown in Figure 4.4. The region of reduced variability is located adjacent to a region of enhanced variability, located in the southern U.S. This suggests, like what is found in the CESM1-CAM4, that variability is displaced from the north central U.S. into the southern U.S. when ENSO is present. The CESM2 results show that ENSO drives a 20% reduction in Z500 variance over the Northern United States and Southern Canada and an increase of 70%, on average, off the west coast and across the southern region of the United States in CESM2. When comparing the results found in the CESM2 percent difference plot, Figure 5.7, with the original figure from the CESM1-CAM4, Figure 4.4, the magnitude of the enhanced regions, off the west coast and across the southern United States, in the CESM1-CAM4 is

stronger and much more spatially confined than what is seen in the CESM2. The region of displacement is also stronger in the CESM1-CAM4 but impacts a larger region over the central United States than what is found in the CESM2.

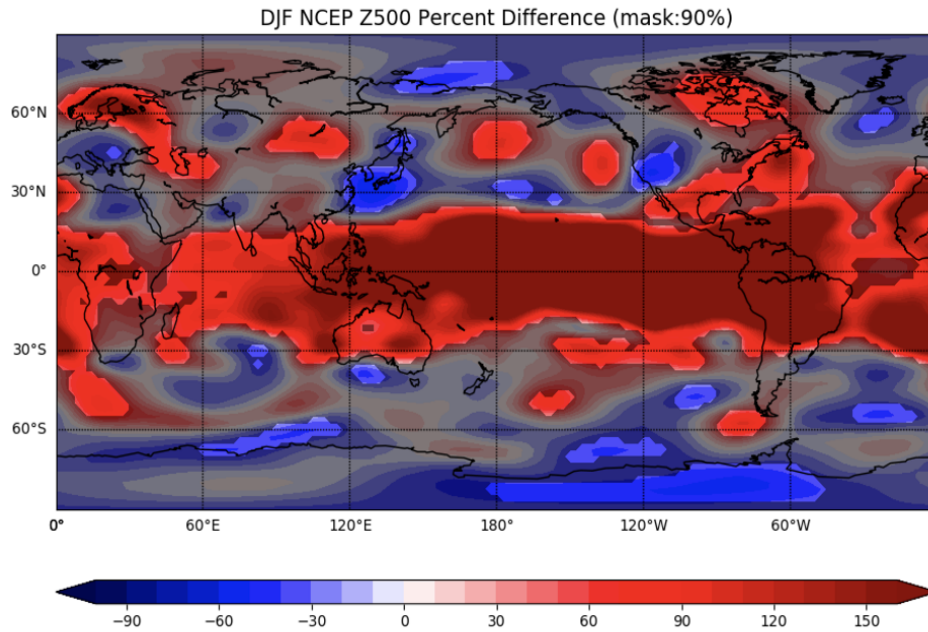


Figure 5.1: NCEP/NCAR reanalysis DJF Z500 percent difference of interannual variance (1950-2020). Comparison between ENSO and neutral events based on a Nino3.4 ENSO threshold of  $\pm 0.5^{\circ}\text{C}$ . Red shading: ENSO increases variability. Blue shading: ENSO displaces variability. Intervals of contours are 10%. Grey shading: Insignificant values based on a 90% confidence level.

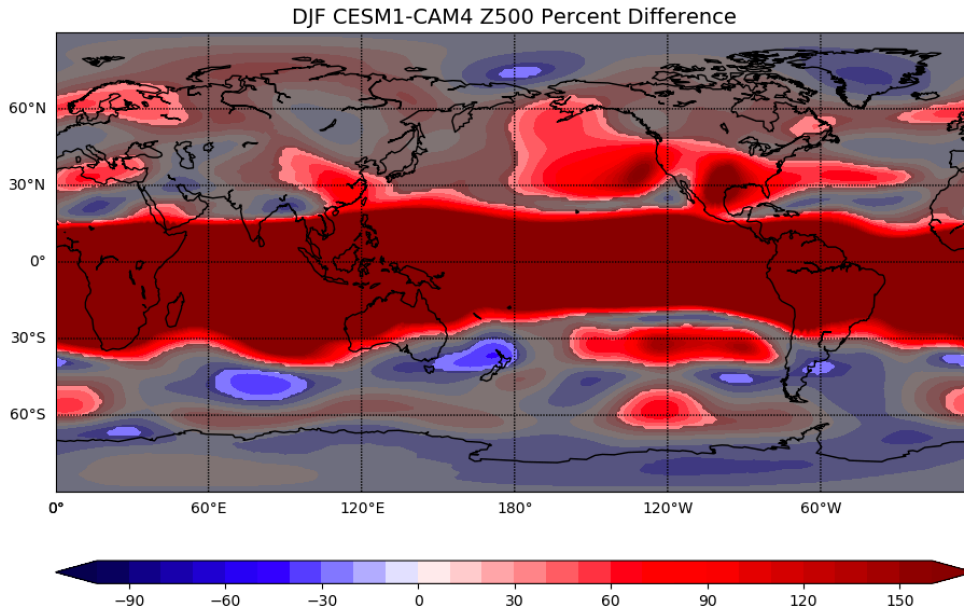


Figure 5.2 CESM1-CAM4 DJF Z500 percent difference of interannual variance. Comparison between CTRL ENSO and Neutral events based on a Nino3.4 ENSO threshold of  $\pm 0.5^{\circ}\text{C}$ . Red shading: ENSO increases variability. Blue shading: ENSO displaces variability. Intervals of contours are 10%. Grey shading: Insignificant values based on a 90% confidence level.

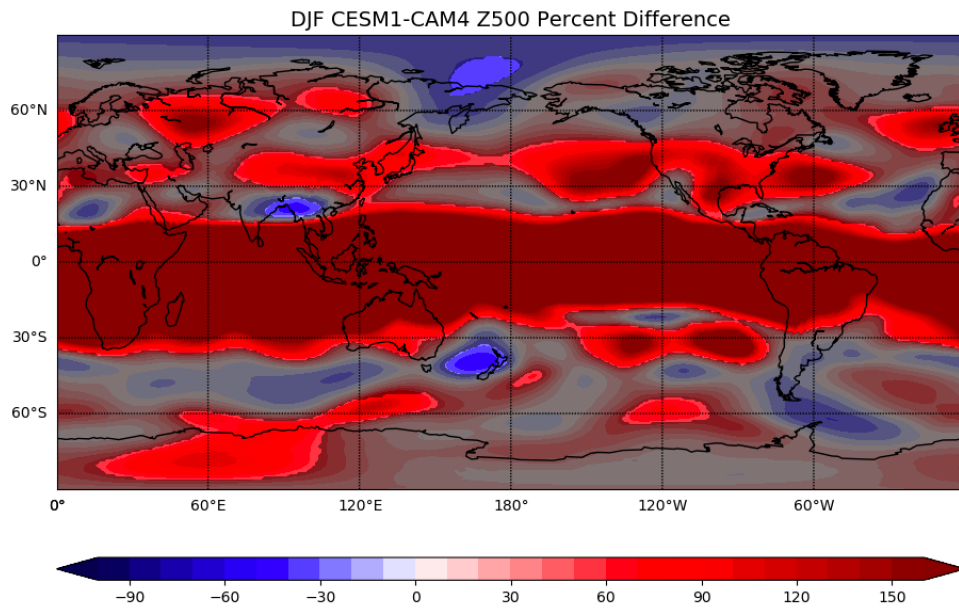


Figure 5.3 CESM1-CAM4 DJF Z500 percent difference of interannual variance. Comparison between CTRL ENSO and Neutral events based on a Nino3.4 ENSO threshold of  $\pm 0.17^{\circ}\text{C}$ , from the NoENSO Nino3.4 standard deviation. Red shading: ENSO increases variability. Blue shading: ENSO displaces variability. Intervals of contours are 10%. Grey shading: Insignificant values based on a 90% confidence level.

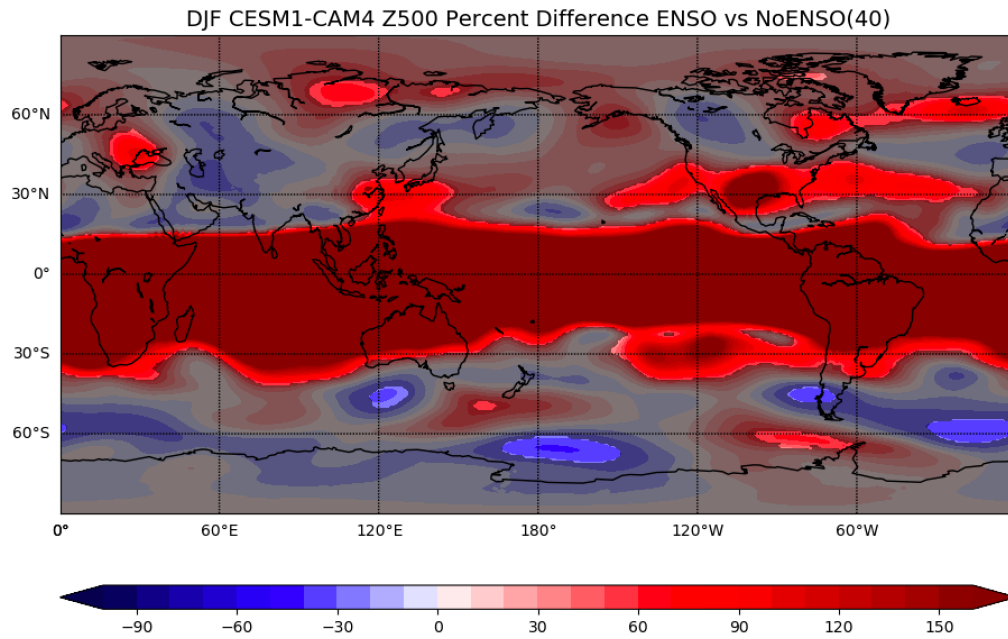


Figure 5.4 CESM1\_CAM4 DJF Z500 percent difference of interannual variance, comparing ENSO and 40 random 40 NoENS(40) DJF years. Red shading: ENSO increases variability. Blue shading: ENSO displaces variability. Intervals of contours are 10%. Grey shading: Insignificant values based on a 95% confidence level.

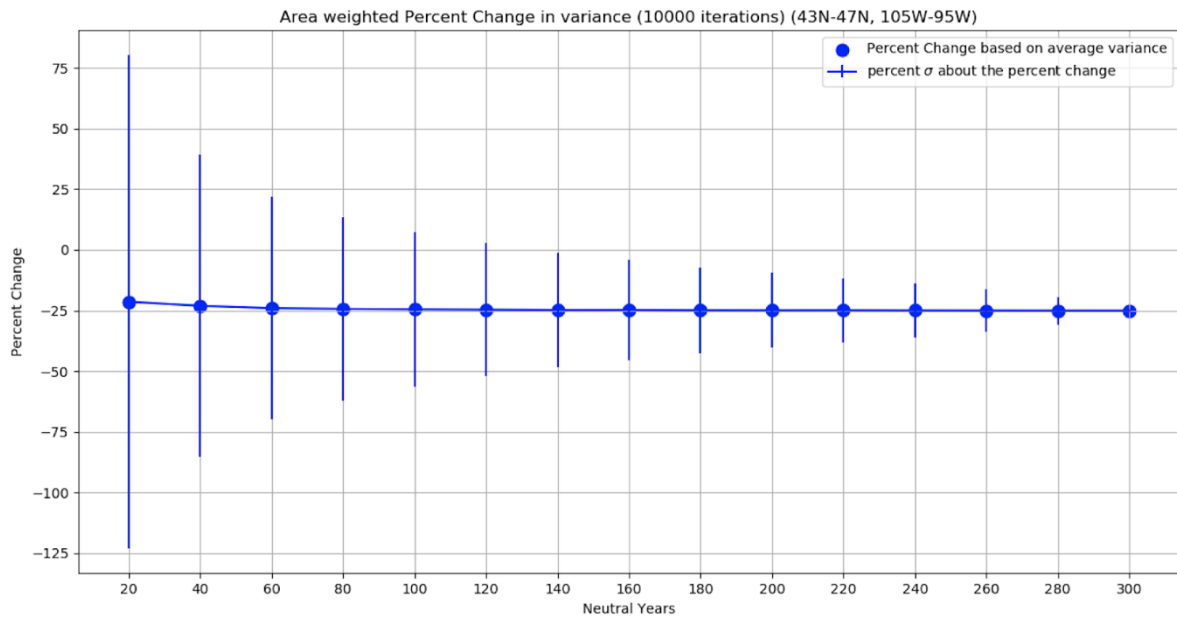


Figure 5.5: Z500 DJF Percent change of average variance over (43°N-47°N,105°W-95°W). Blue dots are the percent change based on the average NoENSO variance, based on 10000 random samples, of a specific sample size. Error bars are the percent uncertainty derived from the standard deviation of individual sample of NoENSO variance. The x-axis is sample sizes of DJF ENSO neutral years. The y-axis is percent change listed as a percentage.

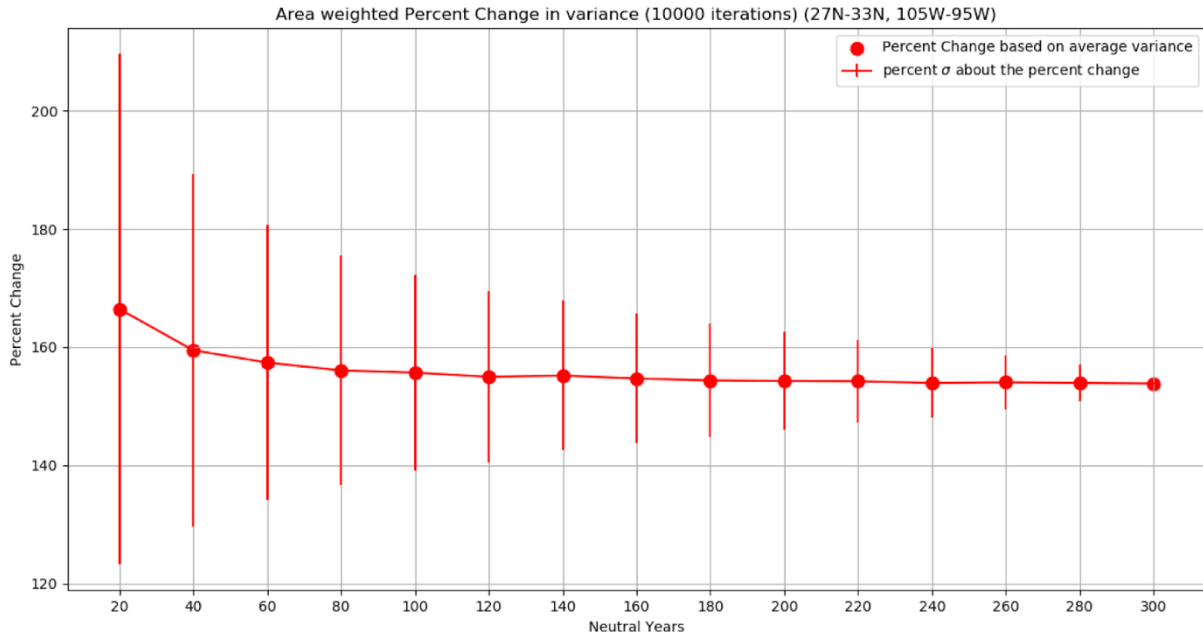


Figure 5.6: Z500 DJF Percent change of average variance over (27°N-33°N,105°W-95°W). Red dots are the percent change based on the average NoENSO variance, based on 10000 random samples, of a specified sample size. Error bars are percent uncertainty derived from the standard deviation of individual sample of NoENSO variance. The x-axis is sample sizes of DJF ENSO neutral years. The y-axis is percent change listed as a percentage.

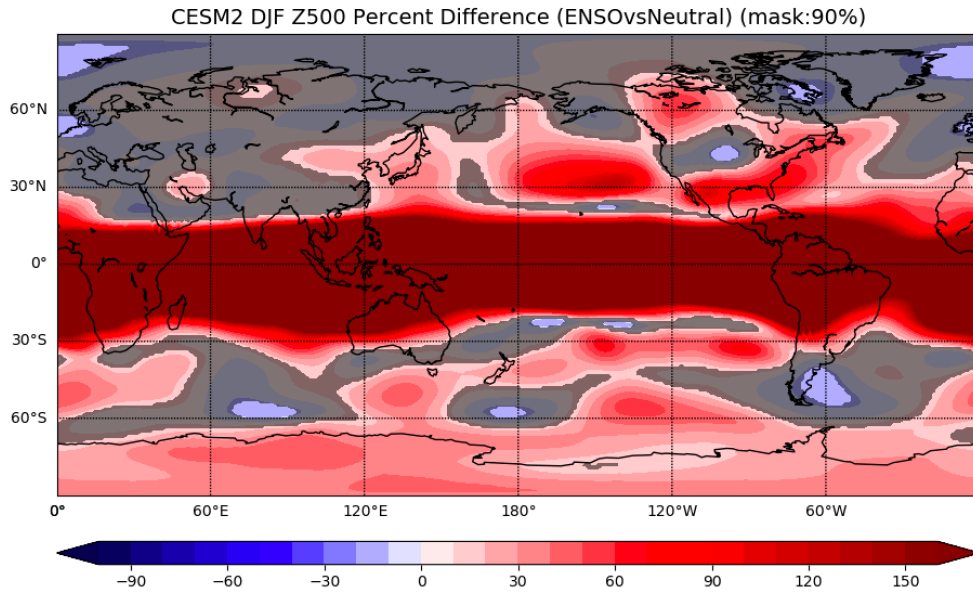


Figure 5.7 CESM2 DJF Z500 percent difference of interannual variance. Comparison between CTRL ENSO and Neutral events based on a Nino3.4 ENSO threshold of  $\pm 0.17^{\circ}\text{C}$ , from the NoENSO Nino3.4 standard deviation. Red shading: ENSO increases variability. Blue shading: ENSO displaces variability. Intervals of contours are 10%. Grey shading: Insignificant values based on a 90% confidence level.

## 6 Discussion

In this study, the ENSO-driven impact of wintertime climate anomalies over North America is investigated. ENSO is the dominant mode of global interannual variability and has been known to enhance the risk of natural, economical, and ecological disasters, such as droughts, floods, low crop yields, and water scarcity. The ENSO-driven impacts over North America are investigated using two coupled model experiments, CTRL and NoENSO. Most previous studies have investigated ENSO-driven impacts through various statistical analyses; however, these approaches are limited by the complexity of ENSO. In this study, a novel modeling approach is used to dynamically suppress the Bjerknes Feedback that supports ENSO variability. This approach involves a partial decoupling of the anomalous wind stress in the equatorial Pacific in the NoENSO experiment. These model experiments, as well as observations, are used to address the following scientific questions:

1. What are the atmospheric and terrestrial impacts of ENSO over North America?
2. Are the same spatial patterns shown in observations as seen in the model results?
3. Are the results found in the CESM1-CAM4 sensitive to the specified ENSO-neutral threshold?
4. How long of a record or simulation length is needed to resolve ENSO's impact on atmospheric variables over North America?

The scientific questions are investigated through comparing the wintertime (DJF) climate anomalies from the CTRL and NoENSO experiments, with emphasis on the Z500, U200 and precipitation. In Z500, three regions of enhanced variability are found over North America. Enhanced variability is found off the west coast of the U.S., across the southern U.S., and in northern Canada, with the most robust increase of variability occurring in the southern U. S. by

155% (Figure 4.4). These regions are expected and well-studied (Wallace and Gutzler, 1981; Trenberth et al., 1998). In the tropics, ENSO enhances variability, as indicated by the monopole-like structures of increased variance. Unexpectedly, we find that ENSO can also reduce climate variability, shown by the regions of blue shading in the percent difference figures (e.g., Figure 4.4, Figure 4.6, Figure 4.8). The largest regions where ENSO reduces variability are seen in the extra-tropics. In these regions, a dipole-like structure is present in the percent difference plots, indicated by regions of increased variance adjacent to regions of reduced variance. This suggests that variability has been displaced from one region (reduced variance region) to another (enhanced variance region). The largest region of displacement, due to ENSO, occurs over the north central region of North America. In this region, ENSO displaces variability to the north and south, as seen in the Z500 DJF El Niño and La Niña composite anomalies (Figure 3.9c-d), resulting in a reduction in variance of approximately 25%. This result is unexpected because with the addition of ENSO forcing, in general, one would expect variability to increase or not be significantly impacted. In precipitation, ENSO reduces variability by 25% in a region south of the Great Lakes and enhances variability by 58% in the southeastern United States, suggesting that ENSO displaces variability to the southeast.

When comparing the 500 hPa geopotential height anomaly results found in the CESM1-CAM4 model with the results from the NCEP/NCAR reanalysis dataset, we find that the spatial pattern over North America is not the same. In the NCEP/NCAR reanalysis percent difference plot (Figure 5.1), ENSO enhances variability in the same three general locations as found in the CESM1-CAM4, but differences exist between the location and amplitude of the displaced region. Next, multiple ENSO neutral thresholds are used to categorize ENSO events in hopes to replicate the resulting spatial pattern found when comparing the model experiments in Z500

(e.g., Figure 4.4). Through this investigation we find that we are unable to replicate the resulting spatial pattern from the model experiments when using ENSO and neutral events from the CTRL experiment. We also find that when the sample size of NoENSO years is limited, a variety of different spatial patterns result when comparing the model experiments. This suggests that a large sample of very neutral years are needed to obtain the amplitude and location of both the enhanced and reduced variance regions over North America found in the comparison between model experiments.

A Monte Carlo random sampling method is used to determine the total number of very ENSO neutral years needed to consistently obtain the amplitude of the percent difference in anomaly variance within 10% uncertainty. For Z500 anomalies, we find that 180 very ENSO neutral years are needed in the enhanced variance region across the southern United States and 240 very ENSO neutral years are needed in the displaced region. In precipitation, we find that 220 very ENSO neutral years are needed in the enhanced region and 240 years are needed to obtain the amplitude within 10% uncertainty in the displaced region. To resolve the variance in both the enhanced and displaced regions for Z500 and precipitation, approximately 240 very ENSO neutral years are needed. Based on the ENSO frequency in the CESM1-CAM4, a minimum simulation length of 1800 years is needed to obtain 240 very ENSO neutral events. These results suggest that the current understanding of ENSO neutral conditions may be incomplete and that the amplitude of the ENSO forced response is in part unknown, given that ENSO neutral conditions are generally under sampled.

To test the hypothesis that 1800 years are needed to resolve ENSO forced response, the CESM2 model is introduced in this study for its 2000-year simulation length and its ability to accurately simulate ENSO teleconnections. Based on the ratio of very ENSO neutral years to

total simulation length in the CESM1-CAM4 CTRL experiment, a simulation length of 2000 years should produce more than the minimum very ENSO neutral years needed. However, we find that only 195 very ENSO neutral years occur in the CESM2 run. This suggests that the total simulation length needed to estimate ENSO forced and non-ENSO related variance is dependent on the periodicity of ENSO events in the model simulation. Therefore, if the frequency of ENSO events is too high in a particular model and ENSO neutral conditions are rare, a longer simulation length will be needed to obtain 240 very ENSO neutral years.

The results from this study show that the current observational record is insufficient to determine if the previously mentioned displacement, found in Z500 and precipitation in the CESM1-CAM4, occurs over North America in nature. Many previous studies have addressed the limitations of exclusively using observational datasets to investigate ENSO forced response (Stevenson et al. 2010; Deser et al. 2017; McKinnon and Deser 2018; Wittenberg 2009). These studies find that the majority of uncertainty in the ENSO forced response found in observations are the result of large internal atmospheric variability. Stevenson et al. (2010) concluded that a simulation length of a minimum of 250 years is needed to obtain stable ENSO statistics. However, based on results found in the present study, a minimum simulation length of at least 1800 years is needed to consistently estimate the ENSO forced variance. We hypothesize that the previously mentioned studies do not resolve the full ENSO neutral variance.

The Monte Carlo sampling approach also shows there is large uncertainty in ENSO neutral variance at small sample sizes (e.g., Figure 5.5, Figure 5.6). This suggests that the typical variability found during an ENSO neutral year, based on the current observation record, is susceptible to a large amount of uncertainty. A potential method of investigating the impact of

uncertainty in ENSO neutral variability is through increasing the ensemble size of seasonal predictions for North American precipitation during ENSO neutral years.

There are a few limitations to the methods presented in this work. Although the CESM1-CAM4 has proven adequate in simulating ENSO and ENSO teleconnections, limitations still exist in the model's ability to replicate the observed frequency and amplitude of ENSO events. For example, if the ratio of ENSO neutral events to ENSO events is higher in a particular model than what is found in CESM1-CAM4, then a simulation length of less than 1800 years may be adequate to resolve the ENSO neutral variance. We expect model results estimating the total number of simulation years needed to resolve ENSO forced variance are dependent on the ENSO statistics of a given model. If the amplitude of SST variability in the equatorial Pacific is overestimated, as in CESM1-CAM4, this could impact the strength of the teleconnective response and overestimate the amplitude of ENSO variability found over North America, impacting the percent difference between ENSO and ENSO neutral years. Previous studies have also shown that climate patterns on longer-timescales can influence ENSO-related predictability (Gershunov and Barnett 1998; Gershunov et al. 1999; Minobe and Mantua 1999). These studies suggest that modes of climate variability on longer-timescales potentially act as a source of predictability for ENSO neutral years (Gershunov and Cayan 2003). A longer simulation length may also be necessary to take into account the impacts of such low frequency variability, which is oftentimes underestimated in climate models (Cheung et al., 2017).

We also acknowledge that the ability to utilize the model experiments in this study to investigate ENSO's impact on a more regional scale is limited by the resolution of the CESM1-CAM4 and the lack of available daily meteorological fields from the NoENSO experiment. ENSO has been shown to influence the seasonal probability distribution functions (PDFs) of

precipitation and temperature on daily scales, particularly on the frequency of daily extreme events found in the tails of the PDFs (Gershunov 1998; Cayan et al. 1999). For this reason, potential future work might include using various surface variables on daily timescales, with finer resolution, to investigate the more small-scale regional impacts of ENSO on the frequency of extreme events, such as heatwaves, cold snaps, heavy precipitation including rain and snowfall, and droughts. An initial step of the investigation would include using the daily data found in the CESM2 to compare the PDFs of precipitation during ENSO and ENSO neutral years, specifically over the enhanced and displaced region in North America found during the DJF wintertime months.

## REFERENCES

- A. G. Barnston, M. Chelliah, & S. B. Goldenberg. (1997). Documentation of a highly ENSO-related SST region in the equatorial Pacific. *Atmos. & Ocean*, 35, 367–383.
- A. T. Wittenberg. (2009). Are historical records sufficient to constrain ENSO simulations? *Geophys. Res. Lett.*, 36, L12702.
- A. T. Wittenberg, A. Rosati, T. L. Delworth, G. A. Vecchi, & F. Zeng. (2014). ENSO modulation: Is it decadal predictable? *J. Climate*, 27, 2667–2681.
- Alexander, M., Bladé, I., Newman, M., Lanzante, J., Lau, N.-C., & Scott, J. (2002). The Atmospheric Bridge: The Influence of ENSO Teleconnections on Air–Sea Interaction over the Global Oceans. *Journal of Climate*, 15(2205–2231).
- Athanasiadis, P. J., Wallace, J. M., & Wettstein, J. J. (2010). Patterns of Wintertime Jet Stream Variability and Their Relation to the Storm Tracks. *Journal of the Atmospheric Sciences*, 67(5), 1361–1381. <https://doi.org/10.1175/2009JAS3270.1>
- BJERKNES, J. (1969). ATMOSPHERIC TELECONNECTIONS FROM THE EQUATORIAL PACIFIC. *Monthly Weather Review*, 97(3), 163–172. [https://doi.org/10.1175/1520-0493\(1969\)097<0163:ATFTEP>2.3.CO;2](https://doi.org/10.1175/1520-0493(1969)097<0163:ATFTEP>2.3.CO;2)
- Bogenschutz, P. A., Gettelman, A., Hannay, C., Larson, V. E., Neale, R. B., Craig, C., & Chen, C.-C. (2018). The path to CAM6: Coupled simulations with CAM5.4 and CAM5.5. *Geoscientific Model Development*, 11(1), 235–255. <https://doi.org/10.5194/gmd-11-235-2018>
- Busalacchi, A. J., Takeuchi, K., & O'Brien, J. J. (1983). Interannual variability of the equatorial Pacific—Revisited. *Journal of Geophysical Research: Oceans*, 88(C12), 7551–7562. <https://doi.org/10.1029/JC088iC12p07551>
- Capotondi, A., Deser, C., Phillips, A. S., Okumura, Y., & Larson, S. M. (2020). ENSO and Pacific Decadal Variability in the Community Earth System Model Version 2. *Journal of Advances in Modeling Earth Systems*, 12(12), e2019MS002022. <https://doi.org/10.1029/2019MS002022>
- Capotondi, A., Wittenberg, A. T., Newman, M., Lorenzo, E. D., Yu, J.-Y., Braconnot, P., Cole, J., Dewitte, B., Giese, B., Guilyardi, E., Jin, F.-F., Karnauskas, K., Kirtman, B., Lee, T., Schneider, N., Xue, Y., & Yeh, S.-W. (2015). Understanding ENSO Diversity. *Bulletin of the American Meteorological Society*, 96(6), 921–938. <https://doi.org/10.1175/BAMS-D-13-00117.1>
- D. R. Cayan, K. T. Redmond, & L. G. Riddle. (1999). *ENSO and hydrologic extremes in the western United States*. 12, 2881–2893.

- Chen, L.-C., van den Dool, H., Becker, E., & Zhang, Q. (2017). ENSO Precipitation and Temperature Forecasts in the North American Multimodel Ensemble: Composite Analysis and Validation. *Journal of Climate*, 30(3), 1103–1125. <https://doi.org/10.1175/JCLI-D-15-0903.1>
- Chen, M., Xie, P., Janowiak, J. E., & Arkin, P. A. (2002). Global Land Precipitation: A 50-yr Monthly Analysis Based on Gauge Observations. *Journal of Hydrometeorology*, 3(3), 249–266. [https://doi.org/10.1175/1525-7541\(2002\)003<0249:GLPAYM>2.0.CO;2](https://doi.org/10.1175/1525-7541(2002)003<0249:GLPAYM>2.0.CO;2)
- Cheung, A. H., Mann, M. E., Steinman, B. A., Frankcombe, L. M., England, M. H., & Miller, S. K. (2017). Comparison of Low-Frequency Internal Climate Variability in CMIP5 Models and Observations. *Journal of Climate*, 30(12), 4763–4776. <https://doi.org/10.1175/JCLI-D-16-0712.1>
- Compo, G., & Sardeshmukh, P. (2010). Removing ENSO-Related Variations from the Climate Record. *Journal of Climate - J CLIMATE*, 23, 1957–1978. <https://doi.org/10.1175/2009JCLI2735.1>
- Danabasoglu, G., Bates, S. C., Briegleb, B. P., Jayne, S. R., Jochum, M., Large, W. G., Peacock, S., & Yeager, S. G. (2012). The CCSM4 Ocean Component. *Journal of Climate*, 25(5), 1361–1389. <https://doi.org/10.1175/JCLI-D-11-00091.1>
- Danabasoglu, G. [National C. for A. R., Boulder, Colorado], Lamarque, J.-F. [NOAA E. S. R. Inst. F. R. in E. S., Univ. of CO. ], Bacmeister, J. T. [University C. for A. R. B. C. 80307 (United S., Bailey, D. [National C. for A. R., DuVivier, A. K. [National C. for A. R., Edwards, J. [National C. for A. R. (NCAR)], Emmons, L. [National C. for A. R., Boulder, CO], Fasullo, J. [University C. for A. R., Garcia, R. R. [National C. for A. R., PO Box 3000-80307,], Gettelman, A. [National C. for A. R., Hannay, C. [National C. for A. R., Holland, M. M. [National C. for A. R., Boulder, Colorado], Large, W. G. [National C. for A. R., Lauritzen, P. H. [National C. for A. R., Lawrence, D. M. [National C. for A. R., Boulder, Colorado], Lenaerts, J. [Utrecht U., Lindsay, K. [National C. for A. R., Lipscomb, W. [Los A. N. L., Mills, M. [University C. for A. R., ... Strand, W. G. [National C. for A. R. (2020). The Community Earth System Model version 2 (CESM2). *Journal of Advances in Modeling Earth Systems*. <https://doi.org/10.1029/2019MS001916>
- Deser, C., Phillips, A., Bourdette, V., & Teng, H. (2012). Uncertainty in climate change projections: The role of internal variability. *Climate Dynamics*, 38(3), 527–546. <https://doi.org/10.1007/s00382-010-0977-x>
- Deser, C., Phillips, A. S., Tomas, R. A., Okumura, Y. M., Alexander, M. A., Capotondi, A., Scott, J. D., Kwon, Y.-O., & Ohba, M. (2012). ENSO and Pacific Decadal Variability in the Community Climate System Model Version 4. *Journal of Climate*, 25(8), 2622–2651. <https://doi.org/10.1175/JCLI-D-11-00301.1>
- Deser, C., Simpson, I. R., McKinnon, K. A., & Phillips, A. S. (2017). The Northern Hemisphere Extratropical Atmospheric Circulation Response to ENSO: How Well Do

We Know It and How Do We Evaluate Models Accordingly? *Journal of Climate*, 30(13), 5059–5082. <https://doi.org/10.1175/JCLI-D-16-0844.1>

Deser, C., Simpson, I. R., Phillips, A. S., & McKinnon, K. A. (2018). How Well Do We Know ENSO's Climate Impacts over North America, and How Do We Evaluate Models Accordingly? *Journal of Climate*, 31(13), 4991–5014. <https://doi.org/10.1175/JCLI-D-17-0783.1>

Ellis, A. W., & Barton, N. P. (2012). Characterizing the North Pacific Jet Stream for Understanding Historical Variability in Western United States Winter Precipitation. *Physical Geography*, 33(2), 105–128. <https://doi.org/10.2747/0272-3646.33.2.105>

Fedorov, A. V., & Philander, S. G. (2001). A Stability Analysis of Tropical Ocean-Atmosphere Interactions: Bridging Measurements and Theory for El Niño. *Journal of Climate*, 14(14), 3086–3101. [https://doi.org/10.1175/1520-0442\(2001\)014<3086:ASAOTO>2.0.CO;2](https://doi.org/10.1175/1520-0442(2001)014<3086:ASAOTO>2.0.CO;2)

Frauen, C., Dommenges, D., Tyrrell, N., Rezný, M., & Wales, S. (2014). Analysis of the Non-Linearity of El Niño Southern Oscillation Teleconnections. *Journal of Climate*, 27. <https://doi.org/10.1175/JCLI-D-13-00757.1>

Gebbie, G., Eisenman, I., Wittenberg, A., & Tziperman, E. (2007). Modulation of Westerly Wind Bursts by Sea Surface Temperature: A Semistochastic Feedback for ENSO. *Journal of the Atmospheric Sciences*, 64(9), 3281–3295. <https://doi.org/10.1175/JAS4029.1>

Gent, P. R., Danabasoglu, G., Donner, L. J., Holland, M. M., Hunke, E. C., Jayne, S. R., Lawrence, D. M., Neale, R. B., Rasch, P. J., Vertenstein, M., Worley, P. H., Yang, Z.-L., & Zhang, M. (2011). The Community Climate System Model Version 4. *Journal of Climate*, 24(19), 4973–4991. <https://doi.org/10.1175/2011JCLI4083.1>

A. Gershunov. (1998). *ENSO influence on intraseasonal extreme rainfall and temperature frequencies in the contiguous United States: Implications for long-range predictability*. 11, 3192–3203.

Gershunov, A., & Cayan, D. R. (2003). Heavy Daily Precipitation Frequency over the Contiguous United States: Sources of Climatic Variability and Seasonal Predictability. *Journal of Climate*, 16(16), 2752–2765. [https://doi.org/10.1175/1520-0442\(2003\)016<2752:HDPFOT>2.0.CO;2](https://doi.org/10.1175/1520-0442(2003)016<2752:HDPFOT>2.0.CO;2)

Gershunov, A., & Barnett, T. P. (1998). Interdecadal Modulation of ENSO Teleconnections. *Bulletin of the American Meteorological Society*, 79(12), 2715–2726. [https://doi.org/10.1175/1520-0477\(1998\)079<2715:IMOET>2.0.CO;2](https://doi.org/10.1175/1520-0477(1998)079<2715:IMOET>2.0.CO;2)

- Gershunov, A., Barnett, T. P., & Cayan, D. R. (1999). North Pacific interdecadal oscillation seen as factor in ENSO-related North American climate anomalies. *Eos, Transactions American Geophysical Union*, 80(3), 25–30. <https://doi.org/10.1029/99EO00019>
- Gill, A. E. (1980). Some simple solutions for heat-induced tropical circulation. *Quarterly Journal of the Royal Meteorological Society*, 106(449), 447–462. <https://doi.org/10.1002/qj.49710644905>
- Golnaraghi, M., & Kaul, R. (1995). The Science of Policymaking: Responding to ENSO. *Environment: Science and Policy for Sustainable Development*, 37(1), 16–44. <https://doi.org/10.1080/00139157.1995.9929210>
- Harrison, D. E., & Larkin, N. K. (1998). Seasonal U.S. temperature and precipitation anomalies associated with El Niño: Historical results and comparison with 1997-98. *Geophysical Research Letters*, 25(21), 3959–3962. <https://doi.org/10.1029/1998GL900061>
- Hoerling, M. P., & Kumar, A. (1997). Why do North American climate anomalies differ from one El Niño event to another? *Geophysical Research Letters*, 24(9), 1059–1062. <https://doi.org/10.1029/97GL00918>
- Hoerling, M. P., Kumar, A., & Zhong, M. (1997). El Niño, La Niña, and the Nonlinearity of Their Teleconnections. *Journal of Climate*, 10(8), 1769–1786. [https://doi.org/10.1175/1520-0442\(1997\)010<1769:ENOLNA>2.0.CO;2](https://doi.org/10.1175/1520-0442(1997)010<1769:ENOLNA>2.0.CO;2)
- Holland, M. M., Bailey, D. A., Briegleb, B. P., Light, B., & Hunke, E. (2012). Improved Sea Ice Shortwave Radiation Physics in CCSM4: The Impact of Melt Ponds and Aerosols on Arctic Sea Ice. *Journal of Climate*, 25(5), 1413–1430. <https://doi.org/10.1175/JCLI-D-11-00078.1>
- Hoskins, B. J., & Ambrizzi, T. (1993). Rossby Wave Propagation on a Realistic Longitudinally Varying Flow. *Journal of Atmospheric Sciences*, 50(12), 1661–1671. [https://doi.org/10.1175/1520-0469\(1993\)050<1661:RWPOAR>2.0.CO;2](https://doi.org/10.1175/1520-0469(1993)050<1661:RWPOAR>2.0.CO;2)
- Hoskins, B. J., & Karoly, D. J. (1981). The Steady Linear Response of a Spherical Atmosphere to Thermal and Orographic Forcing. *Journal of the Atmospheric Sciences*, 38(6), 1179–1196. [https://doi.org/10.1175/1520-0469\(1981\)038<1179:TSLROA>2.0.CO;2](https://doi.org/10.1175/1520-0469(1981)038<1179:TSLROA>2.0.CO;2)
- Huang, B., Thorne, P. W., Banzon, V. F., Boyer, T., Chepurin, G., Lawrimore, J. H., Menne, M. J., Smith, T. M., Vose, R. S., & Zhang, H.-M. (2017). Extended Reconstructed Sea Surface Temperature, Version 5 (ERSSTv5): Upgrades, Validations, and Intercomparisons. *Journal of Climate*, 30(20), 8179–8205. <https://doi.org/10.1175/JCLI-D-16-0836.1>

- Hunke, E. C., W. H. Liscomb, A. K. Turner, N. Jeffery, and S. Elliot (2015), CICE: the Los Alamos Sea Ice Model, Documentation and Software User's Manual, version 5.1. Tech. Rep. LA-CC-06-012, Los Alamos, New Mexico.
- Hurrell, J. W., Holland, M. M., Gent, P. R., Ghan, S., Kay, J. E., Kushner, P. J., Lamarque, J.-F., Large, W. G., Lawrence, D., Lindsay, K., Lipscomb, W. H., Long, M. C., Mahowald, N., Marsh, D. R., Neale, R. B., Rasch, P., Vavrus, S., Vertenstein, M., Bader, D., ... Marshall, S. (2013). The Community Earth System Model: A Framework for Collaborative Research. *Bulletin of the American Meteorological Society*, 94(9), 1339–1360. <https://doi.org/10.1175/BAMS-D-12-00121.1>
- Kalnay, E., Kanamitsu, M., Kistler, R., Collins, W., Deaven, D., Gandin, L., Iredell, M., Saha, S., White, G., Woollen, J., Zhu, Y., Leetmaa, A., Reynolds, B., Chelliah, M., Ebisuzaki, W., Higgins, W., Janowiak, J., Mo, K. C., Ropelewski, C., ... Joseph, D. (1996). The NCEP/NCAR 40-Year Reanalysis Project. *Bulletin of the American Meteorological Society*, 77(3), 437–472. [https://doi.org/10.1175/1520-0477\(1996\)077<textless0437:TNYRP>textgreater2.0.CO;2](https://doi.org/10.1175/1520-0477(1996)077<textless0437:TNYRP>textgreater2.0.CO;2)
- Kiladis, G. N., & Diaz, H. F. (1989). Global Climatic Anomalies Associated with Extremes in the Southern Oscillation. *Journal of Climate*, 2(9), 1069–1090. [https://doi.org/10.1175/1520-0442\(1989\)002<1069:GCAAWE>2.0.CO;2](https://doi.org/10.1175/1520-0442(1989)002<1069:GCAAWE>2.0.CO;2)
- Larson, S. M., & Kirtman, B. P. (2015). Revisiting ENSO Coupled Instability Theory and SST Error Growth in a Fully Coupled Model. *Journal of Climate*, 28(12), 4724–4742. <https://doi.org/10.1175/JCLI-D-14-00731.1>
- Larson, S. M., Kirtman, B. P., & Vimont, D. J. (2017). A Framework to Decompose Wind-Driven Biases in Climate Models Applied to CCSM/CESM in the Eastern Pacific. *Journal of Climate*, 30(21), 8763–8782. <https://doi.org/10.1175/JCLI-D-17-0099.1>
- Larson, S. M., Pegion, K. V., & Kirtman, B. P. (2018). The South Pacific Meridional Mode as a Thermally Driven Source of ENSO Amplitude Modulation and Uncertainty. *Journal of Climate*, 31(13), 5127–5145. <https://doi.org/10.1175/JCLI-D-17-0722.1>
- Larson, S. M., Vimont, D. J., Clement, A. C., & Kirtman, B. P. (2018). How Momentum Coupling Affects SST Variance and Large-Scale Pacific Climate Variability in CESM. *Journal of Climate*, 31(7), 2927–2944. <https://doi.org/10.1175/JCLI-D-17-0645.1>
- Lau, K.-M., Li, P., Sui, C. H., & Nakazawa, T. (1989). Dynamics of Super Cloud Clusters, Westerly Wind Bursts, 30–60 Day Oscillations and ENSO: An Unified View. *Journal of the Meteorological Society of Japan. Ser. II*, 67(2), 205–219. [https://doi.org/10.2151/jmsj1965.67.2\\_205](https://doi.org/10.2151/jmsj1965.67.2_205)
- Lawrence, D. M., Fisher, R. A., Koven, C. D., Oleson, K. W., Swenson, S. C., Bonan, G., Collier, N., Ghimire, B., van Kampenhout, L., Kennedy, D., Kluzek, E., Lawrence, P. J., Li, F., Li, H., Lombardozzi, D., Riley, W. J., Sacks, W. J., Shi, M., Vertenstein, M., ...

- Zeng, X. (2019). The Community Land Model Version 5: Description of New Features, Benchmarking, and Impact of Forcing Uncertainty. *Journal of Advances in Modeling Earth Systems*, 11(12), 4245–4287. <https://doi.org/10.1029/2018MS001583>
- Lawrence, D. M., Oleson, K. W., Flanner, M. G., Thornton, P. E., Swenson, S. C., Lawrence, P. J., Zeng, X., Yang, Z.-L., Levis, S., Sakaguchi, K., Bonan, G. B., & Slater, A. G. (2011). Parameterization improvements and functional and structural advances in Version 4 of the Community Land Model. *Journal of Advances in Modeling Earth Systems*, 3(1). <https://doi.org/10.1029/2011MS00045>
- L’Heureux, M. L., Tippett, M. K., & Barnston, A. G. (2015). Characterizing ENSO Coupled Variability and Its Impact on North American Seasonal Precipitation and Temperature. *Journal of Climate*, 28(10), 4231–4245. <https://doi.org/10.1175/JCLI-D-14-00508.1>
- L’Heureux, M. L., Tippett, M. K., Kumar, A., Butler, A. H., Ciasto, L. M., Ding, Q., Harnos, K. J., & Johnson, N. C. (2017). Strong Relations Between ENSO and the Arctic Oscillation in the North American Multimodel Ensemble. *Geophysical Research Letters*, 44(22), 11,654–11,662. <https://doi.org/10.1002/2017GL074854>
- McKinnon, K. A., & Deser, C. (2018). Internal Variability and Regional Climate Trends in an Observational Large Ensemble. *Journal of Climate*, 31(17), 6783–6802. <https://doi.org/10.1175/JCLI-D-17-0901.1>
- Minobe, S., & Mantua, N. (1999). Interdecadal modulation of interannual atmospheric and oceanic variability over the North Pacific. *Progress in Oceanography*, 43, 163–192. doi:10.1016/S0079-6611(99)00008-7
- Moore, A. M., & Kleeman, R. (1999). Stochastic Forcing of ENSO by the Intraseasonal Oscillation. *Journal of Climate*, 12(5), 1199–1220. [https://doi.org/10.1175/1520-0442\(1999\)012<1199:SFOEBT>2.0.CO;2](https://doi.org/10.1175/1520-0442(1999)012<1199:SFOEBT>2.0.CO;2)
- Neale, R. B., Chen, C. C., Gettelman, A., Lauritzen, P. H., Park, S., Williamson, D. L., et al. (2010). Description of the NCAR Community Atmosphere Model (CAM5.0) (Tech. Rep. NCAR/TN-4861STR). Boulder, CO: National Center for Atmospheric Research.
- Neale, R. B., Richter, J., Park, S., Lauritzen, P. H., Vavrus, S. J., Rasch, P. J., & Zhang, M. (2013). The Mean Climate of the Community Atmosphere Model (CAM4) in Forced SST and Fully Coupled Experiments. *Journal of Climate*, 26(14), 5150–5168. <https://doi.org/10.1175/JCLI-D-12-00236.1>
- Oleson, K., Lawrence, D., B, G., Flanner, M., Kluzek, E., Lawrence, P., Levis, S., Swenson, S., Thornton, E., Feddema, J., Heald, C., Lamarque, J.-F., Niu, G.-Y., Qian, T., Running, S., Sakaguchi, K., Yang, Z.-L., Zeng, X., & Zeng, X. (2010). *Technical Description of version 4.0 of the Community Land Model (CLM)*.

- Pedlow, J. S., Editor, & Miles, J. W., Reviewer. (2004). Waves in the Ocean and Atmosphere: Introduction to Wave Dynamics. *Applied Mechanics Reviews*, 57(4), B20–B20. <https://doi.org/10.1115/1.1786585>
- R. B. Neale, J. H. Richter, & M. Jochum. (2008). The impact of convection on ENSO: From a delayed oscillator to a series of events. *J. Climate*, 21, 5904–5924.
- Reiter, E., & Bierly, G. (2005). Jet Streams. In J. E. Oliver (Ed.), *Encyclopedia of World Climatology* (pp. 435–439). Springer Netherlands. [https://doi.org/10.1007/1-4020-3266-8\\_113](https://doi.org/10.1007/1-4020-3266-8_113)
- Ropelewski, C. F., & Halpert, M. S. (1986). North American Precipitation and Temperature Patterns Associated with the El Niño/Southern Oscillation (ENSO). *Monthly Weather Review*, 114(12), 2352–2362. [https://doi.org/10.1175/1520-0493\(1986\)114<2352:NAPATP>2.0.CO;2](https://doi.org/10.1175/1520-0493(1986)114<2352:NAPATP>2.0.CO;2)
- Ropelewski, C. F., & Halpert, M. S. (1987). Global and Regional Scale Precipitation Patterns Associated with the El Niño/Southern Oscillation. *Monthly Weather Review*, 115(8), 1606–1626. [https://doi.org/10.1175/1520-0493\(1987\)115<1606:GARSPP>2.0.CO;2](https://doi.org/10.1175/1520-0493(1987)115<1606:GARSPP>2.0.CO;2)
- Schwendike, J., Berry, G. J., Reeder, M. J., Jakob, C., Govekar, P., & Wardle, R. (2015). Trends in the local Hadley and local Walker circulations. *Journal of Geophysical Research: Atmospheres*, 120(15), 7599–7618. <https://doi.org/10.1002/2014JD022652>
- Seager, R., Harnik, N., Kushnir, Y., Robinson, W., & Miller, J. (2003). Mechanisms of Hemispherically Symmetric Climate Variability. *Journal of Climate*, 16(18), 2960–2978. [https://doi.org/10.1175/1520-0442\(2003\)016<2960:MOHSCV>2.0.CO;2](https://doi.org/10.1175/1520-0442(2003)016<2960:MOHSCV>2.0.CO;2)
- Seiki, A., & Takayabu, Y. N. (2007). Westerly Wind Bursts and Their Relationship with Intraseasonal Variations and ENSO. Part I: Statistics. *Monthly Weather Review*, 135(10), 3325–3345. <https://doi.org/10.1175/MWR3477.1>
- Soulard, N., Lin, H., & Yu, B. (2019). The changing relationship between ENSO and its extratropical response patterns. *Scientific Reports*, 9(1), 6507. <https://doi.org/10.1038/s41598-019-42922-3>
- Stevenson, S., Fox-Kemper, B., Jochum, M., Rajagopalan, B., & Yeager, S. G. (2010). ENSO Model Validation Using Wavelet Probability Analysis. *Journal of Climate*, 23(20), 5540–5547. <https://doi.org/10.1175/2010JCLI3609.1>
- Su, H., Neelin, J. D., & Meyerson, J. E. (2005). Mechanisms for Lagged Atmospheric Response to ENSO SST Forcing. *Journal of Climate*, 18(20), 4195–4215. <https://doi.org/10.1175/JCLI3514.1>

- Suarez, M. J., & Schopf, P. S. (1988). A Delayed Action Oscillator for ENSO. *Journal of Atmospheric Sciences*, 45(21), 3283–3287. [https://doi.org/10.1175/1520-0469\(1988\)045<3283:ADAOFE>2.0.CO;2](https://doi.org/10.1175/1520-0469(1988)045<3283:ADAOFE>2.0.CO;2)
- Tian, F., Zhang, R.-H., & Wang, X. (2019). A Positive Feedback Onto ENSO Due to Tropical Instability Wave (TIW)-Induced Chlorophyll Effects in the Pacific. *Geophysical Research Letters*, 46(2), 889–897. <https://doi.org/10.1029/2018GL081275>
- Trenberth, K. E., Branstator, G. W., Karoly, D., Kumar, A., Lau, N.-C., & Ropelewski, C. (1998). Progress during TOGA in understanding and modeling global teleconnections associated with tropical sea surface temperatures. *Journal of Geophysical Research: Oceans*, 103(C7), 14291–14324. <https://doi.org/10.1029/97JC01444>
- Wallace, J. M., & Gutzler, D. S. (1981). Teleconnections in the Geopotential Height Field during the Northern Hemisphere Winter. *Monthly Weather Review*, 109(4), 784–812. [https://doi.org/10.1175/1520-0493\(1981\)109<0784:TITGHF>2.0.CO;2](https://doi.org/10.1175/1520-0493(1981)109<0784:TITGHF>2.0.CO;2)
- Worley, P. H., Mirin, A. A., Craig, A. P., Taylor, M. A., Dennis, J. M., & Vertenstein, M. (2011). Performance of the Community Earth System Model. *SC '11: Proceedings of 2011 International Conference for High Performance Computing, Networking, Storage and Analysis*, 1–11. <https://doi.org/10.1145/2063384.2063457>
- Zhang, R.-H., & Levitus, S. (1997). Interannual Variability of the Coupled Tropical Pacific Ocean–Atmosphere System Associated with the El Niño–Southern Oscillation. *Journal of Climate*, 10(6), 1312–1330. [https://doi.org/10.1175/1520-0442\(1997\)010<1312:IVOTCT>2.0.CO;2](https://doi.org/10.1175/1520-0442(1997)010<1312:IVOTCT>2.0.CO;2)